Diagnosing nonlocal effects and coherent structure scales in moist convection using a large-eddy simulation

Fu-Sheng Kao[1], Yi-Hung Kuo[2], and Chien-Ming Wu[1]

[1]National Taiwan University
[2]University of California, Los Angeles

August 22, 2024

Abstract

The anelastic theory of effective buoyancy has been generalized to include the effects of momentum flux convergence. Mediated by the nonlocal perturbation pressure, the dynamics tends to average over details of the forcing, yielding acceleration robust to small-scale variations of the flow. Here we demonstrate in a large-eddy simulation (LES) with a 100-m horizontal grid spacing that including the anelastic nonlocal dynamics can help capture the mean evolution of convection without fully resolving the fine-scale coherent turbulent structures embedded in the flow. Instances of convection in the LES are identified. For these, the buoyancy and dynamic contributions to the vertical momentum tendency are separately diagnosed. The diagnoses show that buoyancy is the leading effect in the vertical acceleration while strongly interacting with the vertical momentum flux convergence. In comparison, the influence of the horizontal momentum flux convergence on the vertical motion are substantially weaker. The sensitivity resulting from averaging over fine-scale features are quantified. For deep-convective cases, these contributions at the cloud scale (~8 km) exhibit a robustness—as measured in a root-mean-square sense—to horizontally smoothing out turbulent features of scales $\lesssim3$ km. As expected, such scales depend on the size of the convective element of interest, while dynamic contributions tend to be more susceptible to horizontal smoothing than does the buoyancy contribution. By verifying a key attribute of the pressure-mediated dynamics in an LES, results here lend support to simplifying the representation of moist convection under the anelastic nonlocal framework for global climate models and storm-resolving simulations.

Diagnosing nonlocal effects and coherent structure scales in moist convection using a large-eddy simulation

Fu-Sheng Kao[1], Yi-Hung Kuo[2*], and Chien-Ming Wu[1]

[1]Department of Atmospheric Sciences, National Taiwan University, Taipei City, Taiwan
[2]Cooperative Institute for Modeling the Earth System, Princeton University, Princeton, NJ, USA

Key Points:

- The anelastic dynamics suggests that the flow acceleration is insensitive to the small-scale variation due to the nonlocal pressure effects
- This is verified by a large-eddy simulation in which the acceleration is robust to the coherent turbulent structures embedded in the flow
- This holds for both the buoyancy and dynamic contributions to the acceleration, and for convective elements including a wide range of scales

*Now at Department of Atmospheric and Oceanic Sciences, University of California, Los Angeles, Los Angeles, CA, USA

Corresponding author: Chien-Ming Wu, mog@as.ntu.edu.tw

Abstract

The anelastic theory of effective buoyancy has been generalized to include the effects of momentum flux convergence. Mediated by the nonlocal perturbation pressure, the dynamics tends to average over details of the forcing, yielding acceleration robust to small-scale variations of the flow. Here we demonstrate in a large-eddy simulation (LES) with a 100-m horizontal grid spacing that including the anelastic nonlocal dynamics can help capture the mean evolution of convection without fully resolving the fine-scale coherent turbulent structures embedded in the flow. Instances of convection in the LES are identified. For these, the buoyancy and dynamic contributions to the vertical momentum tendency are separately diagnosed. The diagnoses show that buoyancy is the leading effect in the vertical acceleration while strongly interacting with the vertical momentum flux convergence. In comparison, the influence of the horizontal momentum flux convergence on the vertical motion are substantially weaker. The sensitivity resulting from averaging over fine-scale features are quantified. For deep-convective cases, these contributions at the cloud scale ($\sim$ 8 km) exhibit a robustness—as measured in a root-mean-square sense—to horizontally smoothing out turbulent features of scales $\lesssim$ 3 km. As expected, such scales depend on the size of the convective element of interest, while dynamic contributions tend to be more susceptible to horizontal smoothing than does the buoyancy contribution. By verifying a key attribute of the pressure-mediated dynamics in an LES, results here lend support to simplifying the representation of moist convection under the anelastic nonlocal framework for global climate models and storm-resolving simulations.

Plain Language Summary

Moist convection is a leading effect in climate dynamics and gives rise to extreme weather events under global warming. Climate adaption and mitigation rely on accurately simulating convection which remains challenging even for state-of-the-art climate models. Recent advances in computing power have permitted high-resolution global models that can partially resolve convective storms. But empirical evidence based on exploratory numerical experiments suggests that the resolution needed for practical climate applications will not become available soon. Latest theoretical studies, on the other hand, point to a possibility that, by properly including the effect of pressure in models, the evolution of convective flows can be reasonably captured without fully resolving the small-scale turbulence. In this work, the theoretically motivated assertion is put to the test against and is substantiated by a realistic simulation of convection. This implies potential for improving the model representation of convection with more feasible resolution options for climate applications.

1 Introduction

Moist convection is essential for the redistribution of heat, moisture, momentum (Houze, 2018), and can greatly impact human society through producing extreme precipitation or inducing heatwaves (Neelin et al., 2022; Y. Zhang & Boos, 2023). The representation of moist convection in global climate models (GCMs) is key to accurately capturing the diurnal variability of precipitation (Covey et al., 2016; Rio et al., 2019; Christopoulos & Schneider, 2021), the onset of convection (Xu et al., 2002; Petch, 2004; Y.-H. Kuo et al., 2020), and mesoscale convective system (MCS) precipitation patterns (Dong et al., 2023). Representing convection in GCMs, however, remains challenging due to insufficient model grid spacings to resolve convective processes (Arakawa, 2004), resulting in biases in simulations and casting uncertainty in climate projections (Randall et al., 2003; Flato et al., 2014; Sinha et al., 2015; Leung et al., 2022).

There have been two common approaches devised for the GCM representation of convection. The first approach couples a GCM with a cloud model with which the effects of subgrid-scale convection are parameterized (Arakawa & Schubert, 1974). For conventional parameterizations, variants of steady plumes have been adapted for cloud models (Yanai et al., 1973; G. J. Zhang & McFarlane, 1995; Bretherton et al., 2004; Siebesma et al., 2007). Alternatively, superparameterization embeds a limited-domain cloud-resolving model (CRM) within each GCM grid cell (Grabowski, 2001; Khairoutdinov et al., 2008; K.-T. Kuo et al., 2020) which produces better variability of convective processes such as the Madden-Julian oscillation (MJO; Benedict & Randall, 2009). The second approach simply uses finer grid spacings to resolve convection (Tomita & Satoh, 2004; Stevens et al., 2024). Recent advances in computing power have enabled cloud-permitting resolutions of a few kilometers for global storm-resolving models (GSRMs; Satoh et al., 2014; Stevens et al., 2019; Wing et al., 2020; Hohenegger et al., 2023) in which improvements are noted in, e.g., the spatial-temporal distribution of precipitation (Hohenegger et al., 2008); the occurrence of extreme rainfall (Chan et al., 2013; Prein et al., 2013; Ban et al., 2014); orographic enhancement of convection (Prein et al., 2016); and the simulation of convective storm organization and propagation in a dynamically consistent manner (Marsham et al., 2013; Weisman et al., 2023). Still, these efforts are more of an exploratory nature and have not yielded satisfactory outcomes for climate applications (Ma et al., 2022; Miura et al., 2023).

While it is straightforward to try to resolve smaller features of interest by refining grid spacing for CRMs (in superparameterization; Grabowski, 2016) and GSRMs—subject to available computing power—the optimal choices of resolution for aspects of convection are yet to be demonstrated (Hohenegger et al., 2020). Prior studies suggested that a horizontal grid spacing $\Delta_h \approx 4$ km could be sufficient for idealized simulations of squall line systems (Weisman et al., 1997) or bulk convergence behavior (Panosetti et al., 2020); capturing the precipitation diurnal cycle would require $\Delta_h \lesssim 2$ km (Yashiro et al., 2016); and accurately reproducing the structural evolution and precipitation of convective storms may need 1-km or sub-kilometers (Miyamoto et al., 2013; Ito et al., 2021). Empirically, the evidence points to even finer grid spacings in both vertical and horizontal that will not soon become feasible for practical climate applications (Jeevanjee & Zhou, 2022; Jenney et al., 2023). As such, traditional parameterizations—preferably with a novel treatment of moist convection—are very much relevant in the foreseeable future for climate projections as well as for a process-level understanding of convection (Schneider et al., 2024).

This raises the question of whether it is possible to capture important aspects of convection without fully resolving the small-scale turbulent features. And, if so, what would be the minimal resolution required for, e.g., simulating deep-convective entities? This manuscript aims to address these questions via a theoretical approach. In doing so, we are motivated by recent studies of effective buoyancy (Tarshish et al., 2018; Y.-H. Kuo & Neelin, 2022; Davies-Jones, 2022) that sought representations of nonhydrostatic pressure effects in convective flows, while leveraging solutions developed in Y.-H. Kuo and Neelin (2024a) and a coordinated large-eddy simulation (LES). Specifically, the analytic expression derived under the anelastic framework indicate that the nonlocal pressure response driven by the buoyancy and momentum flux convergence tends to average over details of the forcing, thus yielding acceleration robust to fine-scale variations of the flow [see Figure 5 in Tarshish et al. (2018), Figure 4 in Y.-H. Kuo and Neelin (2022), and the text therein]. Given the importance of convection as a leading effect in climate change, this theoretical assertion warrants further elaboration aided by realistic simulations of convection, particularly since the robustness of the flow tendency suggests potential for simplifying the representation of the dynamics especially at scales relevant for both large cumulonimbus and MCSs.

Following the groundwork laid in Y.-H. Kuo and Neelin (2024a), here, we diagnose the vertical acceleration within convective regions in an LES and examine the sensitivity of the acceleration to small-scale turbulent features of the flow. As prelude, Section 2 recaps the anelastic nonlocal dynamics, focusing on diagnosing the buoyancy and dynamic contributions to the vertical acceleration. We then briefly overview in Section 3 the setup of the LES experiment in which the acceleration contributions are diagnosed. Section 4 presents the diagnosed vertical mass flux tendency contributions for a selected deep-convective case. The robustness of these contributions to horizontal smoothing for convective features of different sizes are examined in Section 5. Finally, we summarize in Section 6 and discuss potential implications.

2 Anelastic Nonlocal Dynamics: An Overview

To prepare for the analyses presented in subsequent sections, here we follow Y.-H. Kuo and Neelin (2022, 2024a) to recap the diagnostic equation for the nonlocal vertical acceleration. For orientation, note that no approximations are made beyond the anelastic framework in this manuscript.

Assuming the anelastic continuity equation $\nabla\cdot(\rho_0\mathbf{u}) = 0$, where $\rho_0(z)$ is the reference atmospheric density, and $\mathbf{u} \equiv (u, v, w)$ the 3-D velocity field. One can start with the Navier-Stokes equations for $\mathbf{u}$, e.g., Equations 2-4 of Jung and Arakawa (2008)—omitting the eddy ($''$) terms for simplicity—and apply $\nabla\times$ twice to the system; after rearrangement and simplification, the z-component yields

$$\mathcal{L}(a) = \nabla_h^2\left[B - \frac{1}{\rho_0}\nabla\cdot(\rho_0\mathbf{u}w)\right] + D_H, \tag{1}$$

where $a \equiv \partial_t w$ is the Eulerian vertical acceleration, B the buoyancy,

$$\mathcal{L}(a) \equiv \nabla_h^2 a + \frac{\partial}{\partial z}\left[\frac{1}{\rho_0}\frac{\partial}{\partial z}(\rho_0 a)\right], \tag{2}$$

and the higher derivatives of the divergence of horizontal momentum fluxes

$$D_H \equiv \frac{\partial}{\partial z}\left\{\frac{1}{\rho_0}\left[\partial_x\nabla\cdot(\rho_0\mathbf{u}u) + \partial_y\nabla\cdot(\rho_0\mathbf{u}v)\right]\right\}. \tag{3}$$

The buoyancy and dynamic contributions to vertical acceleration can then be diagnosed via Equation 1 as

$$\frac{\partial w}{\partial t} = \underbrace{\mathcal{L}^{-1}\nabla_h^2\left[B \overbrace{- \frac{1}{\rho_0}\nabla\cdot(\rho_0\mathbf{u}w)}^{D_V}\right]}_{a(B)+a(D_V)} \underbrace{+\mathcal{L}^{-1}D_H}_{a(D_H)}, \tag{4}$$

in which $\mathcal{L}^{-1}$ denotes solving Equation 1 with boundary conditions imposed on $\partial_t w$. For simplicity, we use $a(B)$, $a(D_V)$, and $a(D_H)$ to refer to the respective contributions to vertical acceleration by B, D_V, and D_H in subsequent discussion; since ρ_0 is time-independent, we also call $\rho_0 a \equiv \partial_t(\rho_0 w)$ the acceleration and D_V the convergence of vertical momentum, where the meanings are clear from the context.

By comparing Equation 4 here with, e.g., Equation 4 of Jung and Arakawa (2008)—where pressure is expressed in terms of the virtual potential temperature θ_v and *Exner function* π—rearranged as (with c_p the specific heat for air at constant pressure; subscript 0 for a reference state; and prime the respective perturbation)

$$\frac{\partial w}{\partial t} = \underbrace{B - \frac{1}{\rho_0}\nabla\cdot(\rho_0\mathbf{u}w)}_{\textit{Local non-PGF acceleration}} \quad \underbrace{-\frac{\partial}{\partial z}(c_p\theta_{v0}\pi')}_{\textit{PGF}}, \tag{5}$$

we note the following. The elliptic operator $\mathcal{L}(\cdot)$ defined by Equation 2 arises from solving the nonhydrostatic perturbation pressure, and its solution tends to have a vertically and horizontally *nonlocal* influence even if the forcing is localized. This behavior is similar to that seen in, e.g., electrostatics where a point charge can establish an electric field in the surroundings (see also Tarshish et al., 2018). The usage of the term "nonlocal" here, therefore, is different from that in the parameterized up-gradient transport literature (Deardorff, 1966; Holtslag & Moeng, 1991; Siebesma et al., 2007; Zhou et al., 2018; Chor et al., 2021).

On the right-hand side of Equation 4, the first term consists of contributions $a(B)$ and $a(D_V)$ by the buoyancy B and convergence of vertical momentum flux D_V—both of which appear in Equation 5 as the local non-pressure-gradient-force (*non-PGF*) acceleration—that are mediated by the nonlocal perturbation pressure; the second term $a(D_H)$ likewise represents the pressure-driven acceleration resulting from the effect of divergence of horizontal momentum fluxes D_H (recall Equation 3). Thus while Equation 4 appears to be an equation for vertical velocity, it includes the horizontal velocity and continuity equations, and nonlocal effects beyond those represented in *effective buoyancy* [i.e., $a(B)$; see Davies-Jones, 2003; Jeevanjee & Romps, 2016; Peters, 2016].

A key attribute of the nonlocal dynamics is its dependence on dimensions of the convective element (Y.-H. Kuo & Neelin, 2022; Davies-Jones, 2022). Consequently, the solution tends to average over details of the flow, and thus yielding acceleration robust to fine-scale forcing variations. This suggests potential for capturing the evolution of convection without fully resolving the coherent turbulent structures embedded in the flow—the underlying assumption for the simplified representation of the dynamics in the Y.-H. Kuo and Neelin (2024a, 2024b) anelastic convective entity (ACE) model that is yet to be verified quantitatively. To complement and support the theoretical work, this manuscript aims to address the gap by testing the hypothesis using an LES. Specifically, we will examine in the LES the buoyancy and dynamic contributions to vertical acceleration, and quantify their robustness to horizontally smoothing out fine-scale features of the flow.

While it is not possible to cover full treatment here and some aspects of the dynamics must be left for future work, we underlie the following features before turning to the LES setup in the next section. In deriving Equation 4, the eddy terms are omitted for simplicity. Including these would add eddy momentum flux contributions to the dynamic terms D_V, D_H with their impact on the flow exerted through the same mediating pressure effect. In addition, the nonlocal dynamics applies to both the vertical and horizontal acceleration. Recall that Equation 4 (or equivalently, Equation 1) is derived by applying $\nabla\times$ twice to the Navier-Stokes velocity equation and identifying the z-component; the corresponding horizontal component yields an equation akin to Equation 4 from which the horizontal flow tendency can be diagnosed in the same manner.

3 The LES Setup

To diagnose the contributions to vertical acceleration, we use the Vector Vorticity equation cloud-resolving Model or VVM (Jung & Arakawa, 2008; Wu et al., 2019) to produce an LES run. The VVM is a 3-D anelastic model in which the horizontal vorticity is prognostic from which other dynamic variables are inferred; the vertical velocity—being the exception—is directly diagnosed via an elliptic equation with the same operator $\mathcal{L}$ in Equation 2, thus yielding solutions consistent with the diagnostic Equation 4. Such formulation directly couples the flow with buoyancy through vorticity tendency, making the solution responsive to horizontal buoyancy variations for the simulation of convection (see, e.g., K.-T. Kuo & Wu, 2019; Y.-T. Chen & Wu, 2019). In the current implementation, the VVM dynamical core is coupled with additional components including the RRTMG (for radiative transfer; Iacono et al., 2008); the Noah land surface model (F. Chen & Dudhia, 2001); the Shutts and Gray (1994) 1st-order turbulence closure; and the P3 microphysics (Morrison & Milbrandt, 2015; Huang & Wu, 2020). For prior VVM applications, see also Chien and Wu (2016) Hsieh et al. (2022), and Chang et al. (2023).

For the present application, the LES run is performed in a doubly-periodic domain of 102.4 km $\times$ 102.4 km in the horizontal with a flat surface ($z = 0$) and a model top at 19.8 km. The grid spacing is $\Delta x = \Delta y = 100$ m in the horizontal, and Δz increases from 75 m at the surface to 150 m near the model top in the vertical. The simulation is initialized using a tropical oceanic sounding adapted from the DYNAMO campaign observations (Gottschalck et al., 2013). A prescribed large-scale subsidence and a weak background southwesterly of 3 m s^{-1} are imposed (without a meaningful vertical wind shear) so that the solution can capture a variety of convective behaviors including both shallow and deep convection. The imposed southwesterly also results in all convective features propagating northeastward. The simulation period covers 9 days with instantaneous fields output every 10 min—including the buoyancy and dynamic forcings B, D_V, D_H and the respective contributions to vertical acceleration $a(B)$, $a(D_V)$, and $a(D_H)$ diagnosed via Equation 4 during the runtime.

In VVM, the total condensate mixing ratio $q_c \equiv q_\ell + q_i + q_r$ (respectively the mixing ratios of cloud liquid water, ice, and rain) and the buoyancy is evaluated including the virtual effects following

$$B \equiv g \left(\frac{\theta - \theta_0}{\theta_0} + 0.608 q_v - q_c \right), \tag{6}$$

where $g = 9.81$ m s^{-2}; θ is the potential temperature; subscript 0 here for the domain-mean profile; and q_v the water vapor mixing ratio.

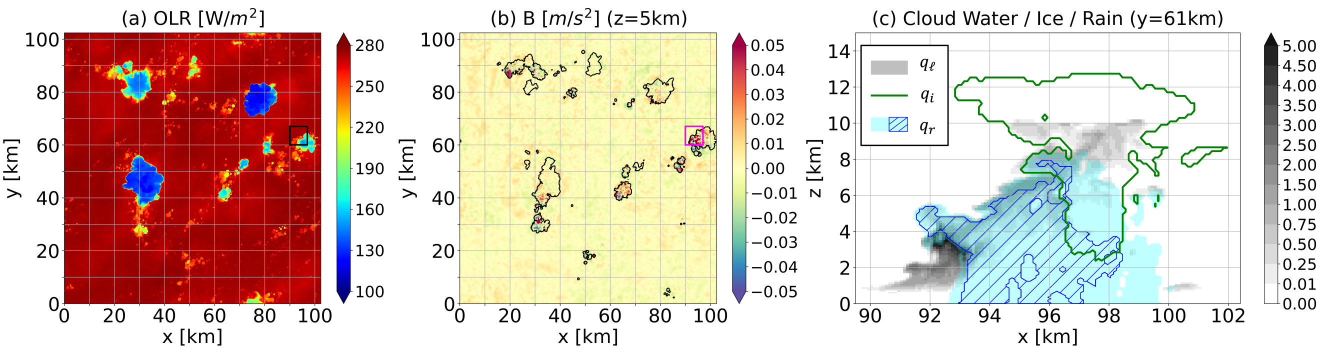

Figure 1. Snapshots at $t = 66$ h 40 m into the VVM simulation for (a) OLR and (b) buoyancy at $z = 5$ km. A developing deep-convective cloud occurs at the boxed location in (a-b) for which the mixing ratios of condensate species at $y = 61$ km are shown in (c), including the cloud liquid water q_ℓ (gray shading in g kg^{-1}), ice q_i (green contours for $q_i = 0.1$ g kg^{-1}), and rain drops q_r (light blue and hatching for q_r exceeding 0.1 and 1 g kg^{-1}, respectively); the total condensate mixing ratio $q_c \equiv q_\ell + q_i + q_r$. Note that a weak background southwesterly is imposed on the solution, resulting in all convective features moving northeastward. The cloud instance in (c) is examined in subsequent figures. The black/magenta square in (a-b) marks a region of 7 km $\times$ 7 km in the horizontal, comparable to the current global storm-resolving resolution, and is used to define the mean tendency $\overline{(\cdot)}$.

To give a sense of the VVM simulation, Figure 1 illustrates snapshots at $t = 66$ h 40 m. The outgoing long-wave radiation (OLR) in Figure 1a shows a number of convective clouds at this time, two of which are mature and exhibit extensive high anvils. A few developing instances can be noted in Figure 1b as indicated by the strong buoyancy anomalies at $z = 5$ km. Among these, one is centered near $x = 93$ km and $y = 63$ km for which Figure 1c shows the cross section of condensate mixing ratios q_ℓ (gray shading in g kg^{-1}), q_i (green contour for 0.1 g kg^{-1}), and q_r (light blue and hatching for values exceeding 0.1 and 1 g kg^{-1}, respectively).

The developing instance illustrated in Figure 1c is selected for a case study with additional diagnoses presented through subsequent Figures 2-6. For another case study sampled at a later time $t = 76$ h 40 m yielding consistent results, see Supporting Information. In these two LES timeslices, we also identify all cloud objects of different sizes (see Appendix C for the identifying criteria). These objects are then used to compile the statistics in Figure 7 for demonstrating the dependence on convective feature size.

We are now ready for diagnosing the contributions to vertical acceleration in the LES.

4 Buoyancy and Dynamic Contributions to Vertical Acceleration

For the selected case highlighted in Figure 1, the buoyancy and dynamic forcings B, D_V, D_H and their respective contributions to vertical mass flux tendency $\rho_0 a(B)$, $\rho_0 a(D_V)$, $\rho_0 a(D_H)$ are shown in Figure 2 (as a visual reference, the liquid and ice cloud boundaries are marked by the black and green contours). While the details included in Figure 2 are informative, the mean tendency over the convective region is also of interest given its implications for, e.g., representations of moist convection in GCMs as well as understanding convective processes in GSRMs. In particular, the mean mass flux profile through continuity determines the far-field inflow towards the convective region (Schiro et al., 2018; Savazzi et al., 2021) and the saturated outflow for stratiform cloud formation (Y.-H. Kuo & Neelin, 2024b). As such, we illustrate in Figure 3 the mean tendency contributions—denoted by $\rho_0 \overline{a(\cdot)}$—over a region of 7 km × 7 km in the horizontal (marked by a square in Figure 1a,b) comparable to a current GSRM grid cell.

In Figure 2a, the cross section shows the primary positive buoyancy feature emerging between $x = 90$ and 97 km in the liquid-cloud region, exhibiting a chain of rising thermals (Varble et al., 2014; Morrison et al., 2020; Peters et al., 2020). Near the surface, a cold pool yields negative values of buoyancy. The convective cold-top negative buoyancy can also be seen near the top of the (ice) cloud (Holloway & Neelin, 2007; Li et al., 2022), likely due to the combined effect of the mixing-driven evaporative cooling (Squires, 1958; Paluch, 1979; Blyth, 1993) and the vertically nonlocal upward acceleration causing adiabatic cooling (Y.-H. Kuo & Neelin, 2022, 2024a). Figure 2d shows the buoyancy-driven vertical mass flux tendency $\rho_0 a(B) \equiv \rho_0 \mathcal{L}^{-1} \nabla_h^2 B$—recall Equation 4—including both the Archimedean buoyancy and its associated perturbation pressure effect. Overall, the sign of the tendency matches that of the buoyancy. But because of the nonlocal dynamics interacting with the surface boundary condition $\partial_t w = 0$, the near-surface tendency tends to have small values despite the cold-pool negative buoyancy. In addition, if one were to overlay Figure 2a,d, the mass flux tendency would appear to be smoother than the buoyancy (see also Figures 4d and 5d).

Figure 2b shows $D_V \equiv -\rho_0^{-1} \nabla \cdot (\rho_0 \mathbf{u} w)$ with the corresponding mass flux tendency $\rho_0 a(D_V) \equiv \mathcal{L}^{-1} \nabla_h^2 D_V$ in Figure 2e. Compared with the buoyancy, both D_V and $\rho_0 a(D_V)$ exhibit smaller-scale features due to sign reversal in velocity in coherent turbulent structures embedded in the flow, e.g., vortex rings associated with rising thermals. Larger values also tend to be confined within the cloud. While the magnitude in Figure 2b,e appears to be stronger than that of the buoyancy, substantial cancellation can occur when the forcing/tendency is averaged over the cloud region.

Finally, Figure 2c,f illustrates the cross sections of D_H and $\rho_0 a(D_H) \equiv \mathcal{L}^{-1} D_H$. Recall Equation 3 that D_H includes higher derivatives of the divergence of horizontal momentum fluxes, hence has units different from those of B and D_V. This also results in D_H exhibiting even finer-scale features than D_V in Figure 2b. The corresponding $\rho_0 a(D_H)$ in Figure 2f seems less noisy than D_H due to the nonlocal effect.

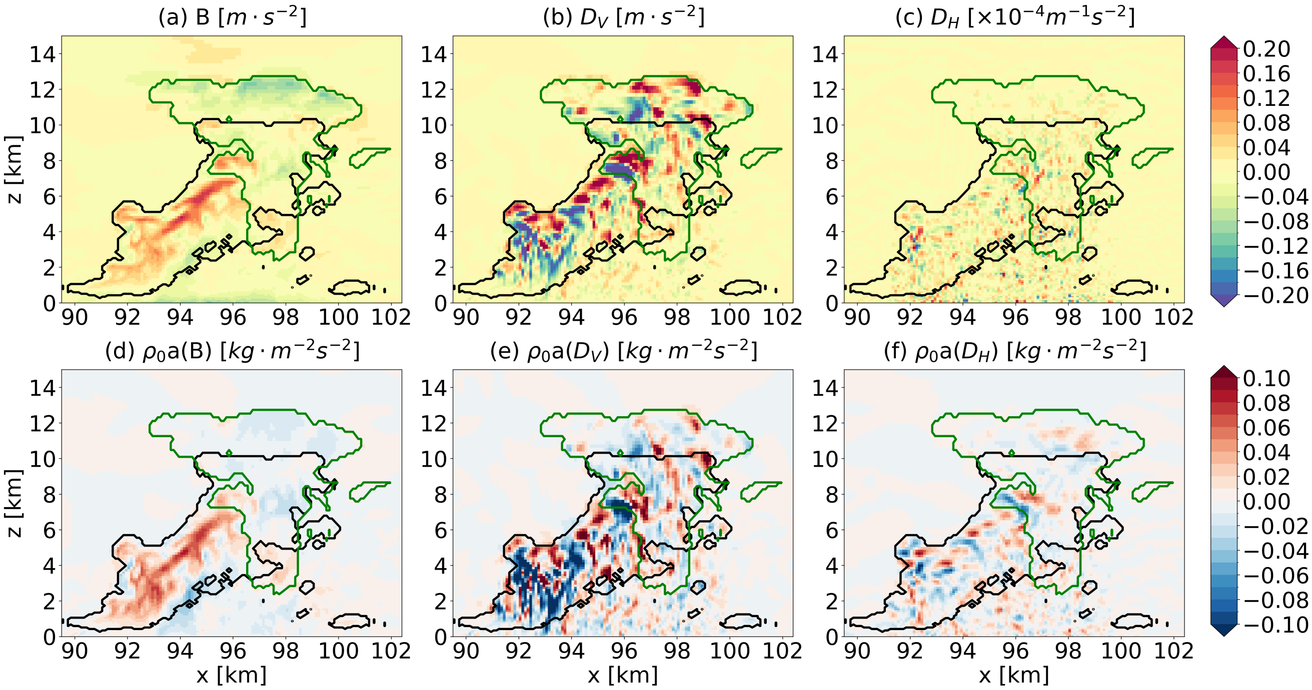

Figure 2. The buoyancy and dynamic forcings that yield the nonlocal vertical acceleration, including contributions by (a) the buoyancy (B), (b) the vertical (D_V) and (c) horizontal momentum flux divergence (D_H); the respective vertical mass flux tendencies $\rho_0 a(B)$, $\rho_0 a(D_V)$, and $\rho_0 a(D_H)$ are in (d-f). Note that the units of D_H in (c) are different from those for (a-b). Cross sections here are sampled from $y = 61$ km at $t = 66$ h 40 m into the VVM simulation, with the black/green contours marking the liquid/ice cloud boundaries as shown in Figure 1c.

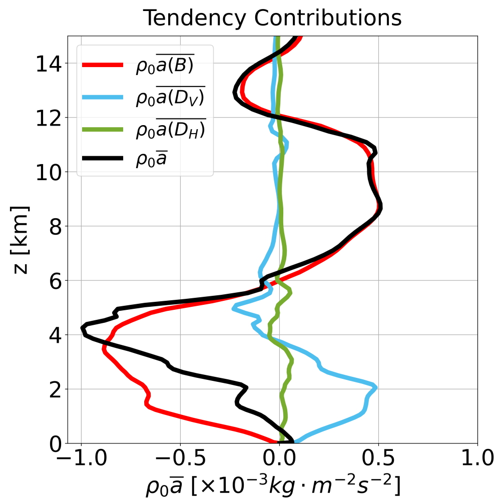

Figure 3. The individual and total contributions to the vertical mass flux tendency horizontally averaged over a 7 km × 7 km region (see the black/magenta square in Figure 1a,b). Solutions here are for the same case illustrated in Figure 2.

The overall magnitude of $\rho_0 a(D_H)$ is notably weaker than $\rho_0 a(B)$, $\rho_0 a(D_V)$ in Figure 2d,e. This is also demonstrated by Figure 3 in which these terms are horizontally averaged over a 7 km $\times$ 7 km box enclosing the convective region indicated by strong buoyancy. The total mean tendency (black line) is dominated by the buoyancy contribution (red), exhibiting an upward acceleration between $z = 6$ and 12 km and a downward tendency above and below. That $\partial_t \partial_z(\rho_0 \overline{w}) = \partial_z(\rho_0 \overline{a}) > 0$ for $4 < z < 8$ km implies the far-field inflow towards the convective region is strengthening (or equivalently, the outflow is weakening) in the mid-troposphere. The dynamic contribution has a modest impact on the total tendency—mostly through D_V (blue). In contrast, the effect of D_H (green) appears to be negligible.

For another deep-convective case examined in the same manner, see Supporting Information. While the precise distributions of the forcing and tendency can vary from case to case, the relative importance of B, D_V, and D_H noted here seems to hold in general.

Next, we turn to the robustness of the vertical mass flux tendency to fine-scale features of the flow.

5 Robustness to Coherent Turbulent Structure

This section focuses on the robustness of the nonlocal dynamics. Specifically, we test the assertion that the evolution of convection can be captured without fully resolving the turbulent flow structures. To this end, we apply a horizontal Gaussian filter to the forcing to even out features finer than a prescribed *smoothing scale* s, and then examine the sensitivity of the nonlocal acceleration to the smoothing. For more details on Gaussian smoothing, see Appendix B.

5.1 Dependence on horizontal smoothing scale

Figure 4 shows the cross sections of B, D_V, D_H and their filtered counterparts denoted by $\widetilde{(\cdot)}$. The column on the left repeats Figure 2a-c and the middle two columns illustrate results filtered with $s = 0.9$ and 2.4 km. The rightmost column includes the mean forcing profiles averaged over the 7 km $\times$ 7 km region—the same used for Figure 3—for selected values of s (results before smoothing are included and labeled as 100m). The corresponding contributions to vertical mass flux tendency are shown in Figure 5.

As noted earlier, the buoyancy includes scales comparable to the size of the cloud in which the coherent structures are embedded (Figure 4a), thus exhibiting a robustness to smoothing (Figure 4b-c). Even with $s = 2.4$ km, the filtered buoyancy $\widetilde{B}$ shows a pattern resembling the original snapshot before filtering. When these are horizontally averaged over the 7 km $\times$ 7 km region, the resulting profiles in Figure 4d are virtually indistinguishable from the original until s well exceeds 3 km. These findings hold for the buoyancy-driven tendency in Figure 5a-d as well. In addition, it is worth reiterating that the nonlocal dynamics applies not only horizontally but also vertically, as is demonstrated by the profiles in Figure 5d tending to be smoother than those of the buoyancy in Figure 4d.

In comparison with buoyancy, the dynamic contributions in Figure 4e-l and Figure 5e-l include features of smaller scales hence are more susceptible to smoothing. While deviations of the filtered results become substantial for larger values of s ($\gtrsim 2.4$ km), the mean profiles—especially for the vertical mass flux tendencies in Figure 5h,l—remain robust in both the horizontal and vertical.

The dependence on smoothing of the total and individual contributions to the mass flux tendency is summarized in Figure 6 by showing $\|\rho_0\overline{a(\cdot)} - \rho_0\overline{a(\widetilde{\cdot})}\|_2 / \|\rho_0\overline{a(\cdot)}\|_2$—the normalized root-mean-square (RMS) difference between the mean tendency profiles before and after filtering—as a function of s. Here $\|\cdot\|_2$ denotes the Euclidean norm, and the difference is normalized (using the norm before filtering) so that the value would not

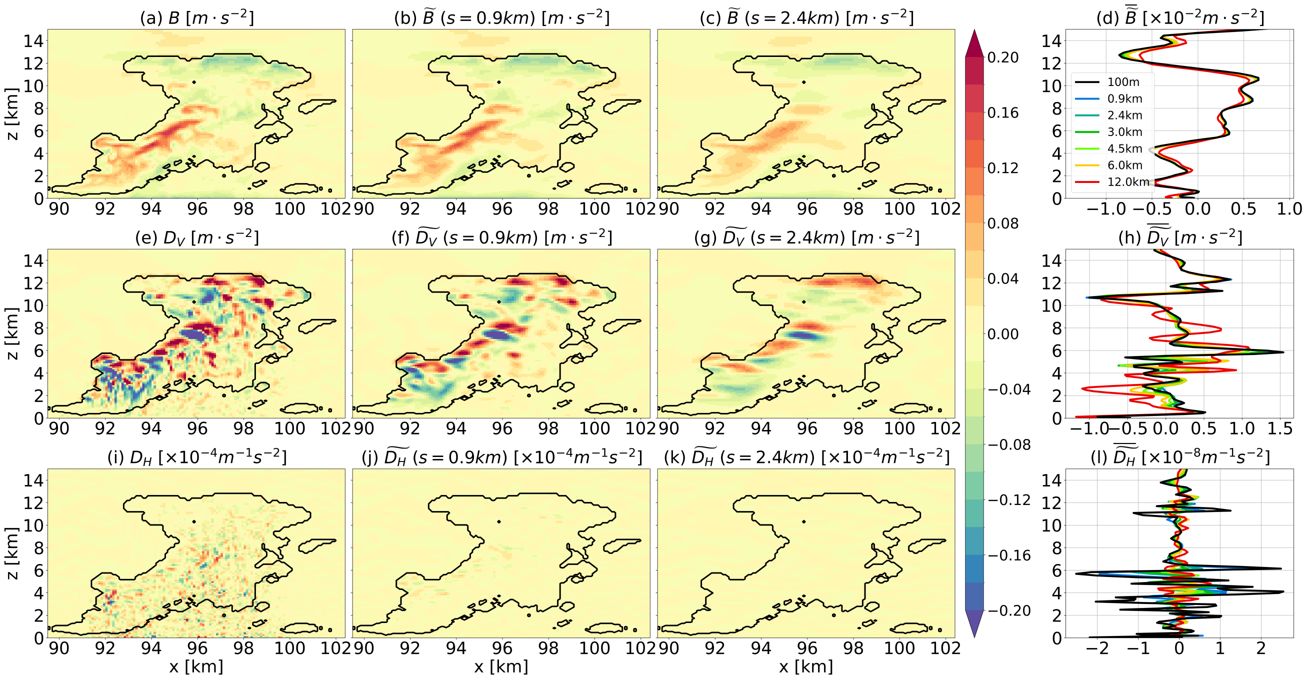

Figure 4. The dependence of the buoyancy and dynamic forcing contributions to horizontal smoothing. (a) The VVM snapshot of buoyancy B as in Figure 2a and (b-c) the horizontally-smoothed buoyancy field $\widetilde{B}$ using a 2-D Gaussian filter with smoothing scales $s = 0.9$ nd 2.4 km to remove the coherent turbulent structure embedded in the flow; the mean profiles of B (black line) and $\widetilde{B}$ (colored lines; for a few values of s in km) horizontally averaged over the 7 km $\times$ 7 km box (see Figure 1a-b) are summarized in (d). (e-h) Same as (a-d) but for the dynamic contribution D_V by the vertical momentum flux convergence; (i-l) Same as (e-h) but for D_H associated with horizontal momentum flux convergence. Note that in (d), (h) and (l) results before smoothing are marked as 100m in the legend.

be impacted by the magnitude of individual contributions. For the selected case, filtering yields solutions with small deviations for the total tendency (black line) and buoyancy contribution (red line) while the dynamic terms (blue and green lines) are less robust with substantially larger deviations. Despite the deviation is most notable for the D_H-induced tendency, the magnitude of the tendency is small and thus tends to have a limited impact on the flow evolution.

5.2 Cloud-size dependence and morphology

Two important aspects have to be considered as we move from the selected example to a variety of instances of convection. First, the robustness of the mean tendency profiles seen in Figure 5d,h,l is not an artifact arising from the interaction between the convolution $\widetilde{(\cdot)}$ and horizontal averaging $\overline{(\cdot)}$. The smoothing scale $s \sim 3$ km at which the deviations of the filtered solutions start to pick up is not sensitive to the size of the domain (e.g., 7 km $\times$ 7 km) over which the horizontal mean is computed (not shown). Instead, this threshold scale varies primarily with the forcing morphology as demonstrated by Figure 6: the threshold tends to be larger for forcing with a simple structure (e.g., B in Figure 4a) while distributions having multiple extrema across a short distance (D_V,

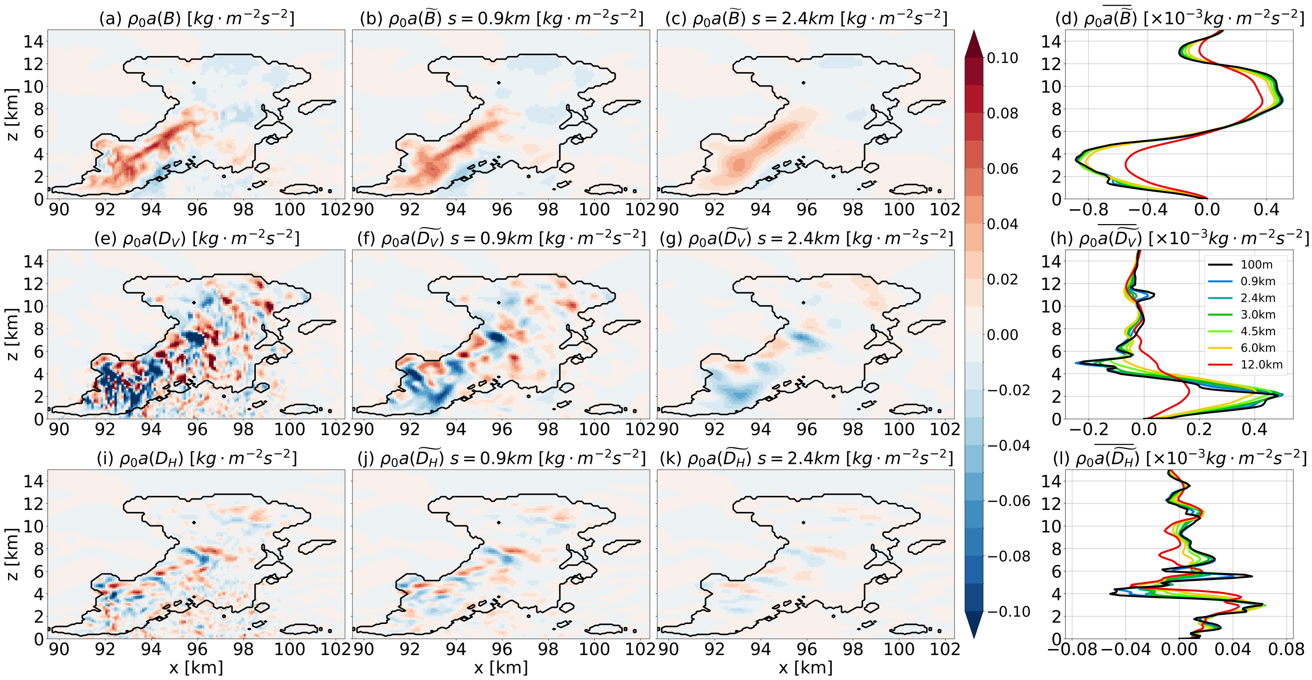

Figure 5. Same as Figure 4 but showing the respective vertical mass flux tendency.

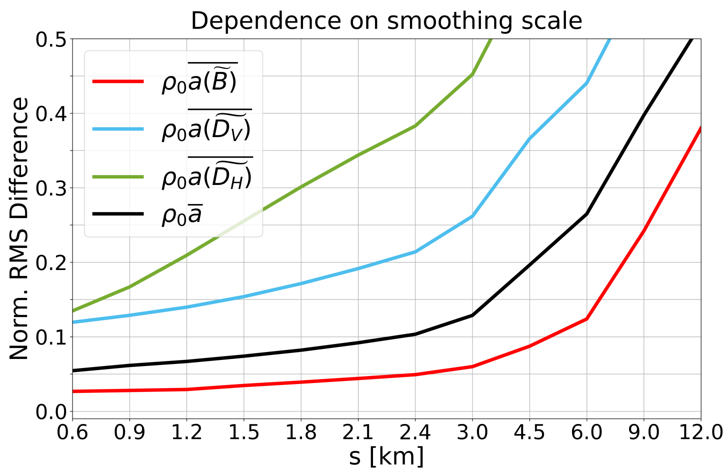

Figure 6. Normalized root-mean-square (RMS) differences between the mean profiles of the VVM vertical mass flux tendency $\rho_0\overline{a(\cdot)}$ and the horizontally-smoothed tendency $\rho_0\overline{a(\widetilde{\cdot})}$, contributed by the individual and total forcings. Here, the differences are normalized by the RMS of the tendency profiles $\rho_0\overline{a(\cdot)}$ before smoothing. Note that the x-axis here showing selected values of s is not on a linear scale.

D_H in Figure 4e,i) tend to yield a smaller threshold. Second, the dependence on cloud size must be assessed.

To address this, Figure 7 repeats the analysis displayed in Figure 6 for a collection of 185 cloud samples of different sizes identified in two LES timeslices that are 10 hours apart at $t = 66$ h 40 m and 76 h 40 m (see Appendix C for the identifying criteria and

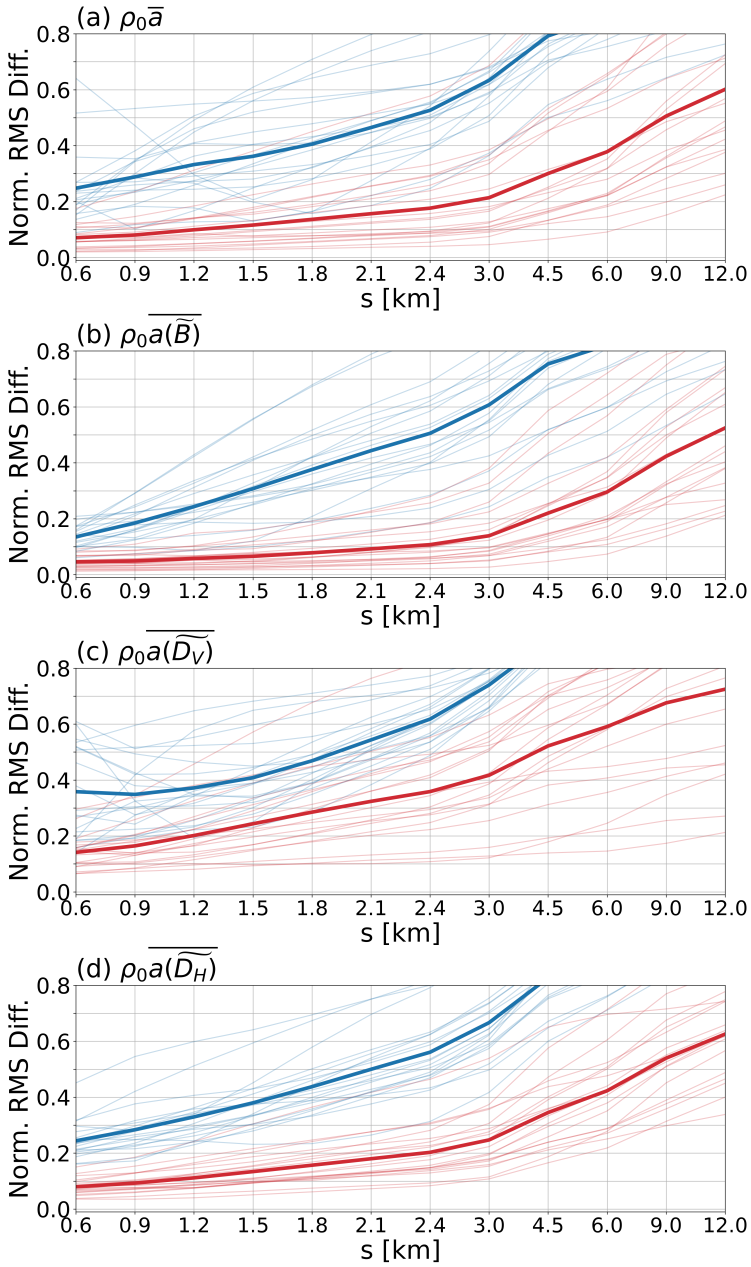

Figure 7. Same as Figure 6, illustrating for an ensemble of clouds of different horizontal sizes (see Appendix C for the measure of size). The light red lines show the dependence of the normalized RMS difference on the smoothing scale for individual cloud instances whose size is in the top 10% ($\geq$ 7.8 km), while the results for the bottom 10% ($\leq$ 0.8 km) are in light blue. The thick red and blue lines represent the respective means for each category.

the proxy used to measure the cloud size). The normalized RMS differences for the tendency contributions are shown as a function of the smoothing scale for individual clouds in the top (light red lines) and bottom 10% (light blue lines) of the size distribution, together with their respective means for each size group (thick red/blue lines; the 10th- and 90th-percentiles of the cloud size are 0.8 and 7.8 km). The total and buoyancy contributions tend to exhibit smaller differences due to smoothing than do the dynamic contributions; and larger cloud objects systematically yield smaller differences than smaller ones. While fine-scale variations not accounted for by the size proxy can give rise to deviation from the mean, results here are consistent with our intuition built upon earlier illustrations.

6 Summary and Discussion

Under the anelastic framework, this manuscript examines the vertical acceleration field mediated by the nonlocal perturbation pressure. The buoyancy and dynamic contributions to the acceleration are diagnosed in an LES of 100-m horizontal grid spacing that simulates a variety of convective features. For these, the buoyancy contribution $a(B)$—known as the effective buoyancy (Davies-Jones, 2003)—tends to dominate the evolution of the mean flow while interacting with the *effective dynamic acceleration* $a(D_V)$ (Y.-H. Kuo & Neelin, 2024a) of a comparable magnitude driven by the convergence of vertical momentum flux. The contribution $a(D_H)$ associated with divergence of horizontal momentum fluxes, in contrast, is at least an order smaller in magnitude thus only has a limited impact on the mean flow.

Results compiled with cloud objects sampled from the LES indicate that the diagnosed contributions to the vertical acceleration tend to be robust to horizontally filtering out fine-scale variations embedded in the flow. Because larger convective entities include coherent structures of larger scales than do smaller clouds, the nonlocal acceleration resulting from larger entities is less susceptible to the smoothing. This is demonstrated by the mean acceleration profiles for selected deep-convective cases exhibiting little variation, measured in root-mean-square differences, before and after the horizontal filtering until the smoothing scale exceeds a threshold of ~ 3 km. As expected, the threshold is systematically smaller for convective features of smaller sizes though deviations from the mean may be seen among individual instances. Also, dynamic contributions exhibit more sensitivity to smoothing than the buoyancy contribution. Although we have focused on the mean tendencies over convective regions, the effect of smaller-scale eddies on tracer transport cannot be overlooked (Jeevanjee & Zhou, 2022; Jenney et al., 2023); the scales associated with coherent flows noted here could facilitate a more consistent treatment for partitioning the mean-flow and eddy contributions.

While the analysis framework in this manuscript is purely diagnostic, it could aid in understanding convective processes for simplified representations in GCMs and GSRMs. Y.-H. Kuo and Neelin (2024b) have illustrated that the approximation $\partial_t w \approx a(B) + a(D_V)$ [i.e., omitting $a(D_H)$] in time-varying solutions for convective updraft tends to spawn off a chain of rising thermals especially in the upper part of the updraft—results here support the use of such approximation. It follows as a corollary that steady plumes are unlikely to be an effective description for convective drafts. Apart from contributing to the overall mixing, the spontaneously-generated thermals can also act as a source of gravity waves in a manner that differs from a steady-updraft solution for parameterized processes such as gravity wave drag (Kim et al., 2003; Beres et al., 2004; Alexander et al., 2021). More generally, the representations of moist/shallow convection in a GCM or GSRM should begin to move away from typical steady-state assumption, or to at least consider these time-dependent aspects.

In addition, horizontal size has recently been recognized as a key factor distinguishing small cloud embryos that grow into deep convection from those do not (Powell, 2024). A greater embryo size favors convective growth by simultaneously reducing entrainment mixing and enhancing the nonlocal effects (Y.-H. Kuo & Neelin, 2024a); solutions here can help discern the relative importance of these two pathways. Including a background wind shear or vorticity can substantially alter the flow evolution (Peters et al., 2019; LeBel & Markowski, 2023; Peters et al., 2023) but its interaction with the nonlocal dynamics will be an endeavor for future work. The onset of convective aggregation is another subject of interest for which the up-gradient transport of boundary layer moist static energy (MSE) due to virtual temperature effect is a leading contribution (Yang, 2018; Huang & Wu, 2022); diagnoses presented here might provide useful ways to quantify the transfers of MSE helping clarify the mechanism.

In light of the results, the point here is not so much about a particular threshold scale, but that aspects of the evolution of convection can be represented without fully resolving the turbulent flow. This inherent feature of the anelastic nonlocal dynamics previously noted in theoretical studies such as Tarshish et al. (2018), Y.-H. Kuo and Neelin (2022), and Davies-Jones (2022) now has an LES underpinning supporting process-level modeling of convection for GCMs and GSRMs.

Appendix A An alternative diagnostic equation for (p, T)-system

This work relies on the VVM LES in which (π, θ) is used in lieu of pressure p and temperature T (Jung & Arakawa, 2008), and thus our presentation of the nonlocal diagnostic equation follows the same approach. The corresponding equation for the alternative (p, T) anelastic system has been covered in Y.-H. Kuo and Neelin (2024a) which is included for completeness:

$$\partial_t(\rho_0 w) = \nabla^{-2}\nabla_h^2\big[\rho_0 B - \nabla\cdot(\rho_0\mathbf{u}w)\big] + \nabla^{-2}D'_H, \tag{A1}$$

where

$$D'_H \equiv \partial_z\big[\partial_x\nabla\cdot(\rho_0\mathbf{u}u) + \partial_y\nabla\cdot(\rho_0\mathbf{u}v)\big]. \tag{A2}$$

The operator $\mathcal{L}$ defined via Equation 2 is replaced by a 3-D Laplacian ∇^2 here with ∇^{-2} denoting solving the Poisson equation. While the change of variables yields simpler expressions, it does not inherently alter the nonlocal dynamics.

Appendix B Gaussian smoothing

To test the robustness of the nonlocal acceleration, in Section 5 we apply a horizontal convolution to filter out fine-scale features of the flow (similar to the smoothing procedure in Shchepetkin & McWilliams, 1998). Specifically, for a variable $f(x, y, z)$ of interest, the filtered field is given by

$$\widetilde{f}(x, y, z) \equiv \iint G(x', y')f(x - x', y - y', z)dx'dy', \tag{B1}$$

where

$$G(x, y) \equiv \frac{1}{2\pi\sigma^2}e^{-(x^2+y^2)/2\sigma^2} \tag{B2}$$

is the 2-D Gaussian kernel. For a given $\sigma > 0$, $G(x, y)$ drops to $\sim 1\%$ of its peak value for $r \equiv \sqrt{x^2 + y^2} \approx 3\sigma$. Hence features smaller than the *smoothing scale* $s \equiv 6\sigma$ tend to be filtered out by the convolution—s is used as a measure for the horizontal smoothing for results included in Section 5.

Note that convolution is a linear operation, thus preserves the relation between the forcing and acceleration contributions, i.e., $a(\widetilde{\cdot}) = \widetilde{a(\cdot)}$. For instance, applying a Gaussian filter with $s = 0.9$ km to the $\rho_0 a(B)$ illustrated in Figure 5a would yield a smoothed solution $\rho_0\widetilde{a(B)}$ that is identical to the $\rho_0 a(\widetilde{B})$ in Figure 5b; the identity holds for the D_V and D_H contributions as well. In principle, this property holds for other linear filters among which the *boxcar* filter corresponding to coarse-graining may be of interest. Nonetheless, we note that (1) the Gaussian smoothing and coarse-graining *should* yield similar results; and (2) the spectral property of the boxcar function *could* produce spurious computational artifacts when the filtering is followed by solving an elliptic equation. As such, the Gaussian smoothing is used for simplicity.

In Figures 4-7, the filtered results are computed by first evaluating B, D_V, D_H via Equations 3-4 and 6 using the LES output, and then applying the Gaussian smoothing. An alternative procedure—as is commonly applicable to considerations of subgrid-scale representations (Leonard, 1975; Moeng, 1984)—applies the Gaussian smoothing to the LES output before computing the forcings. This yields

$$\begin{aligned} \widetilde{D_V}' &\equiv -\frac{1}{\rho_0}\nabla\cdot(\rho_0\tilde{\mathbf{u}}\tilde{w}), \\ \widetilde{D_H}' &\equiv \frac{\partial}{\partial z}\left\{\frac{1}{\rho_0}\left[\partial_x\nabla\cdot(\rho_0\tilde{\mathbf{u}}\tilde{u})+\partial_y\nabla\cdot(\rho_0\tilde{\mathbf{u}}\tilde{v})\right]\right\}, \end{aligned} \tag{B3}$$

which can subsequently be substituted into Equation 4 in lieu of D_V, D_H to solve for the acceleration contributions (for completeness, buoyancy is omitted from Equation B3 since its expression does not include nonlinear terms, hence filtering first does not alter the outcome). It is worth noting that the two filtering procedures yield reasonably consistent outcomes, as demonstrated in Figure B1 which compares the two procedures by showing results for the primary contribution $B + D_V$.

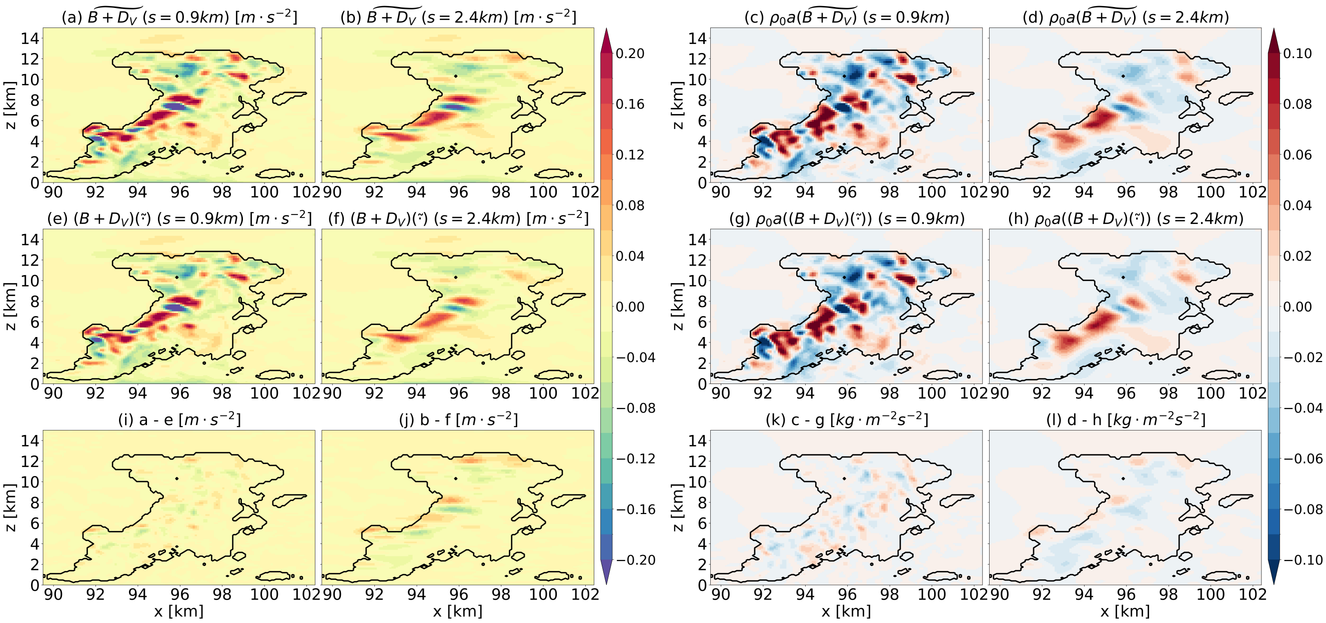

Figure B1. Differences in the smoothed forcing and vertical mass flux tendency due to the filtering procedures. (a-d) Smoothed variables by applying the filter after evaluating $B + D_V$ from the raw LES output. (e-h) The corresponding results computed by applying the filter first using Equation B3. (i-l) Respective differences between (a-d) and (e-h).

In Figure B1, the first row includes the smoothed forcing and vertical mass flux tendency computed by applying the filter after evaluation (i.e., the same procedure for Figures 4-5) while the second row exhibits results for applying the filter first (that is, Equation B3); their differences are illustrated in the bottom row (e.g., Figure B1i shows the difference between panels a and e). In short, while the deviation tends to increase with the smoothing scale, the outcome demonstrates only a modest sensitivity to the filtering procedures.

Appendix C Identifying cloud objects

To infer the relationship between feature size and the robustness of the nonlocal dynamics to smoothing, we identify cloud objects from the LES timeslices and diagnose for each cloud object the buoyancy and dynamic contributions to vertical flow acceleration. The identifying criteria are as follows.

Recall in, e.g., Figure 1a,b that mature clouds with extensive anvils are not necessarily associated with a strong buoyancy or flow velocity. Hence to focus on cases presenting strong forcings, we define a (liquid) cloud object as a connected component of $q_\ell > 0$ in which $w > 5$ m s^{-1} for at least one LES grid point. Each object identified this way is then enclosed by a rectangular column; denoting by A the minimal horizontal area of such columns with which $\sqrt{A}$ is used as a proxy for the object size. This proxy is used to compile the cloud size distribution for the statistics shown in Figure 7 for which the mean mass flux tendencies $\rho_0\overline{a(\cdot)}$ are averaged over the minimal horizontal area A.

Acknowledgments

This work was supported by the Princeton AOS Postdoctoral Research Scientists Program under award NA18OAR4320123 from the National Oceanic and Atmospheric Administration, U.S. Department of Commerce (YHK), and by the National Science and Technology Council of Taiwan through Grants 113-2111-M-002-001- to National Taiwan University (FSK and CMW). We are grateful for comments from Drs. Wei-Ting Chen, Leo J. Donner, James C. McWilliams, and J. David Neelin that helped improve this work.

Data Availability Statement

The VVM source code is publicly available at https://github.com/chienmingwu/VVM, and the LES output can be accessed via https://doi.org/10.5281/zenodo.13317028 together with the analysis and plotting scripts for this manuscript.

References

Alexander, M. J., Liu, C. C., Bacmeister, J., Bramberger, M., Hertzog, A., & Richter, J. H. (2021). Observational validation of parameterized gravity waves from tropical convection in the Whole Atmosphere Community Climate Model. *Journal of Geophysical Research: Atmospheres*, *126*(7), e2020JD033954.

Arakawa, A. (2004). The cumulus parameterization problem: Past, present, and future. *Journal of Climate*, *17*(13), 2493 - 2525.

Arakawa, A., & Schubert, W. H. (1974). Interaction of a cumulus cloud ensemble with the large-scale environment, Part I. *Journal of Atmospheric Sciences*, *31*(3), 674–701.

Ban, N., Schmidli, J., & Schär, C. (2014). Evaluation of the convection-resolving regional climate modeling approach in decade-long simulations. *Journal of Geophysical Research: Atmospheres*, *119*(13), 7889–7907.

Benedict, J. J., & Randall, D. A. (2009). Structure of the madden–julian oscillation in the superparameterized cam. *Journal of the Atmospheric Sciences*, *66*(11), 3277–3296.

Beres, J. H., Alexander, M. J., & Holton, J. R. (2004). A method of specifying the gravity wave spectrum above convection based on latent heating properties and background wind. *Journal of the atmospheric sciences*, *61*(3), 324–337.

Blyth, A. M. (1993). Entrainment in cumulus clouds. *Journal of Applied Meteorology and Climatology*, *32*(4), 626–641.

Bretherton, C. S., McCaa, J. R., & Grenier, H. (2004). A new parameterization for shallow cumulus convection and its application to marine subtropical cloud-topped boundary layers. Part I: Description and 1D results. *Monthly Weather Review*, *132*(4), 864–882.

Chan, S. C., Kendon, E. J., Fowler, H. J., Blenkinsop, S., Ferro, C. A., & Stephenson, D. B. (2013). Does increasing the spatial resolution of a regional climate model improve the simulated daily precipitation? *Climate dynamics*, *41*, 1475–1495.

Chang, Y.-H., Chen, W.-T., Wu, C.-M., Kuo, Y.-H., & Neelin, J. D. (2023). Identifying the deep-inflow mixing features in orographically-locked diurnal convection. *Geophysical Research Letters*, *50*(10), e2023GL103107.

Chen, F., & Dudhia, J. (2001). Coupling an advanced land surface–hydrology model with the Penn State–NCAR MM5 modeling system. Part I: Model implementation and sensitivity. *Monthly weather review*, *129*(4), 569–585.

Chen, Y.-T., & Wu, C.-M. (2019). The role of interactive SST in the cloud-resolving simulations of aggregated convection. *Journal of Advances in Modeling Earth Systems*, *11*(10), 3321–3340.

Chien, M.-H., & Wu, C.-M. (2016). Representation of topography by partial steps using the immersed boundary method in a vector vorticity equation model (VVM). *Journal of Advances in Modeling Earth Systems*, *8*(1), 212-223.

Chor, T., McWilliams, J. C., & Chamecki, M. (2021). Modifications to the K-profile parameterization with nondiffusive fluxes for Langmuir turbulence. *Journal of Physical Oceanography*, *51*(5), 1503–1521.

Christopoulos, C., & Schneider, T. (2021). Assessing biases and climate implications of the diurnal precipitation cycle in climate models. *Geophysical Research Letters*, *48*(13), e2021GL093017.

Covey, C., Gleckler, P. J., Doutriaux, C., Williams, D. N., Dai, A., Fasullo, J., … Berg, A. (2016). Metrics for the diurnal cycle of precipitation: Toward routine benchmarks for climate models. *Journal of Climate*, *29*(12), 4461–4471.

Davies-Jones, R. (2003). An expression for effective buoyancy in surroundings with horizontal density gradients. *Journal of the Atmospheric Sciences*, *60*(23), 2922–2925.

Davies-Jones, R. (2022). An analytical solution of the effective-buoyancy equation. *Journal of the Atmospheric Sciences*, *79*(12), 3135–3144.

Deardorff, J. W. (1966). The counter-gradient heat flux in the lower atmosphere and in the laboratory. *Journal of the Atmospheric Sciences*, *23*(5), 503–506.

Dong, W., Zhao, M., Ming, Y., Krasting, J. P., & Ramaswamy, V. (2023). Simulation of united states mesoscale convective systems using gfdl's new high-resolution general circulation model. *Journal of Climate*, *36*(19), 6967 - 6990.

Flato, G., Marotzke, J., Abiodun, B., Braconnot, P., Chou, S. C., Collins, W., … others (2014). Evaluation of climate models. In *Climate change 2013: the physical science basis. Contribution of Working Group I to the Fifth Assessment Report of the Intergovernmental Panel on Climate Change* (pp. 741–866). Cambridge University Press.

Gottschalck, J., Roundy, P. E., Schreck III, C. J., Vintzileos, A., & Zhang, C. (2013). Large-scale atmospheric and oceanic conditions during the 2011–12 DYNAMO field campaign. *Monthly Weather Review*, *141*(12), 4173–4196.

Grabowski, W. W. (2001). Coupling cloud processes with the large-scale dynamics using the cloud-resolving convection parameterization (CRCP). *Journal of the Atmospheric Sciences*, *58*(9), 978–997.

Grabowski, W. W. (2016). Towards global large eddy simulation: Super-parameterization revisited. *Journal of the Meteorological Society of Japan. Ser. II*, *94*(4), 327–344.

Hohenegger, C., Brockhaus, P., & Schar, C. (2008). Towards climate simulations at cloud-resolving scales. *Meteorologische Zeitschrift*, *17*(4), 383–394.

Hohenegger, C., Korn, P., Linardakis, L., Redler, R., Schnur, R., Adamidis, P., … Stevens, B. (2023). ICON-Sapphire: simulating the components of the Earth system and their interactions at kilometer and subkilometer scales. *Geoscientific Model Development*, *16*(2), 779–811.

Hohenegger, C., Kornblueh, L., Klocke, D., Becker, T., Cioni, G., Engels, J. F., ... Stevens, B. (2020). Climate statistics in global simulations of the atmosphere, from 80 to 2.5 km grid spacing. *Journal of the Meteorological Society of Japan. Ser. II*, *98*(1), 73–91.

Holloway, C. E., & Neelin, J. D. (2007). The convective cold top and quasi equilibrium. *Journal of the Atmospheric Sciences*, *64*(5), 1467–1487.

Holtslag, A. A. M., & Moeng, C.-H. (1991). Eddy diffusivity and countergradient transport in the convective atmospheric boundary layer. *Journal of the Atmospheric Sciences*, *48*(14), 1690–1698.

Houze, R. A. (2018). 100 years of research on mesoscale convective systems. *Meteorological Monographs*, *59*, 17–1.

Hsieh, M.-K., Chen, Y.-W., Chen, Y.-C., & Wu, C.-M. (2022). The roles of local circulation and boundary layer development in tracer transport over complex topography in central Taiwan. *Journal of the Meteorological Society of Japan. Ser. II*, *100*(3), 555–573.

Huang, J.-D., & Wu, C.-M. (2020). Effects of microphysical processes on the precipitation spectrum in a strongly forced environment. *Earth and Space Science*, *7*(6), e2020EA001190.

Huang, J.-D., & Wu, C.-M. (2022). A framework to evaluate convective aggregation: Examples with different microphysics schemes. *Journal of Geophysical Research: Atmospheres*, *127*(5), e2021JD035886.

Iacono, M. J., Delamere, J. S., Mlawer, E. J., Shephard, M. W., Clough, S. A., & Collins, W. D. (2008). Radiative forcing by long-lived greenhouse gases: Calculations with the AER radiative transfer models. *Journal of Geophysical Research: Atmospheres*, *113*(D13).

Ito, J., Tsuguchi, H., Hayashi, S., & Niino, H. (2021). Idealized high-resolution simulations of a back-building convective system that causes torrential rain. *Journal of the Atmospheric Sciences*, *78*(1), 117–132.

Jeevanjee, N., & Romps, D. M. (2016). Effective buoyancy at the surface and aloft. *Quarterly Journal of the Royal Meteorological Society*, *142*(695), 811–820.

Jeevanjee, N., & Zhou, L. (2022). On the resolution-dependence of anvil cloud fraction and precipitation efficiency in radiative-convective equilibrium. *Journal of Advances in Modeling Earth Systems*, *14*(3), e2021MS002759.

Jenney, A. M., Ferretti, S. L., & Pritchard, M. S. (2023). Vertical resolution impacts explicit simulation of deep convection. *Journal of Advances in Modeling Earth Systems*, *15*(10), e2022MS003444.

Jung, J.-H., & Arakawa, A. (2008). A three-dimensional anelastic model based on the vorticity equation. *Monthly Weather Review*, *136*(1), 276–294.

Khairoutdinov, M., DeMott, C., & Randall, D. (2008). Evaluation of the simulated interannual and subseasonal variability in an AMIP-style simulation using the CSU multiscale modeling framework. *Journal of Climate*, *21*(3), 413–431.

Kim, Y.-J., Eckermann, S. D., & Chun, H.-Y. (2003). An overview of the past, present and future of gravity-wave drag parametrization for numerical climate and weather prediction models. *Atmosphere-Ocean*, *41*(1), 65–98.

Kuo, K.-T., Wei-Ting, C., & Chien-Ming, W. (2020). Effects of convection-SST interactions on the South China Sea summer monsoon onset in a multiscale modeling framework model. *TAO: Terrestrial, Atmospheric and Oceanic Sciences*, *31*(2), 2.

Kuo, K.-T., & Wu, C.-M. (2019). The precipitation hotspots of afternoon thunderstorms over the Taipei Basin: Idealized numerical simulations. *Journal of the Meteorological Society of Japan. Ser. II*, *97*(2), 501–517.

Kuo, Y.-H., & Neelin, J. D. (2022). Conditions for convective deep inflow. *Geophysical Research Letters*, *49*, e2022GL100552.

Kuo, Y.-H., & Neelin, J. D. (2024a). Anelastic Convective Entities. Part 1: Formulation and implication for nighttime convection. *Authorea Preprints*.

Kuo, Y.-H., & Neelin, J. D. (2024b). Anelastic Convective Entities. Part 2: Adjustment processes and convective cold top. *Authorea Preprints*.

Kuo, Y.-H., Neelin, J. D., Booth, J. F., Chen, C.-C., Chen, W.-T., Gettelman, A., ... Zhao, M. (2020). Convective transition statistics over tropical oceans for climate model diagnostics: GCM evaluation. *Journal of Atmospheric Sciences*, *77*, 379-403.

LeBel, L. J., & Markowski, P. M. (2023). An analysis of the impact of vertical wind shear on convection initiation using large-eddy simulations: Importance of wake entrainment. *Monthly Weather Review*, *151*(7), 1667–1688.

Leonard, A. (1975). Energy cascade in large-eddy simulations of turbulent fluid flows. In *Advances in Geophysics* (Vol. 18, pp. 237–248). Elsevier.

Leung, L. R., Boos, W. R., Catto, J. L., A. DeMott, C., Martin, G. M., Neelin, J. D., ... others (2022). Exploratory precipitation metrics: Spatiotemporal characteristics, process-oriented, and phenomena-based. *Journal of Climate*, *35*(12), 3659–3686.

Li, Y.-X., Neelin, J. D., Kuo, Y.-H., Hsu, H.-H., & Yu, J.-Y. (2022). How close are leading tropical tropospheric temperature perturbations to those under convective quasi equilibrium? *Journal of the Atmospheric Sciences*, *79*(9), 2307–2321.

Ma, H.-Y., Klein, S. A., Lee, J., Ahn, M.-S., Tao, C., & Gleckler, P. J. (2022). Superior daily and sub-daily precipitation statistics for intense and long-lived storms in global storm-resolving models. *Geophysical Research Letters*, *49*(8), e2021GL096759.

Marsham, J. H., Dixon, N. S., Garcia-Carreras, L., Lister, G. M. S., Parker, D. J., Knippertz, P., & Birch, C. E. (2013). The role of moist convection in the West African monsoon system: Insights from continental-scale convection-permitting simulations. *Geophysical Research Letters*, *40*(9), 1843–1849.

Miura, H., Suematsu, T., Kawai, Y., Yamagami, Y., Takasuka, D., Takano, Y., ... Masumoto, Y. (2023). Asymptotic matching between weather and climate models. *Bulletin of the American Meteorological Society*, *104*(12), E2308 - E2315.

Miyamoto, Y., Kajikawa, Y., Yoshida, R., Yamaura, T., Yashiro, H., & Tomita, H. (2013). Deep moist atmospheric convection in a subkilometer global simulation. *Geophysical Research Letters*, *40*(18), 4922-4926.

Moeng, C.-H. (1984). A large-eddy-simulation model for the study of planetary boundary-layer turbulence. *Journal of the Atmospheric Sciences*, *41*(13), 2052–2062.

Morrison, H., & Milbrandt, J. A. (2015). Parameterization of cloud microphysics based on the prediction of bulk ice particle properties. Part I: Scheme description and idealized tests. *Journal of the Atmospheric Sciences*, *72*(1), 287–311.

Morrison, H., Peters, J. M., Varble, A. C., Hannah, W. M., & Giangrande, S. E. (2020). Thermal chains and entrainment in cumulus updrafts. Part I: Theoretical description. *Journal of the Atmospheric Sciences*, *77*(11), 3637–3660.

Neelin, J. D., Martinez-Villalobos, C., Stechmann, S. N., Ahmed, F., Chen, G., Norris, J. M., ... Lenderink, G. (2022). Precipitation extremes and water vapor: Relationships in current climate and implications for climate change. *Current Climate Change Reports*, *8*(1), 17–33.

Paluch, I. R. (1979). The entrainment mechanism in Colorado cumuli. *Journal of Atmospheric Sciences*, *36*(12), 2467–2478.

Panosetti, D., Schlemmer, L., & Schär, C. (2020). Convergence behavior of idealized convection-resolving simulations of summertime deep moist convection over land. *Climate Dynamics*, *55*(1), 215–234.

Petch, J. C. (2004). The predictability of deep convection in cloud-resolving simulations over land. *Quarterly Journal of the Royal Meteorological Society*, *130*(604), 3173-3187.

Peters, J. M. (2016). The impact of effective buoyancy and dynamic pressure forcing on vertical velocities within two-dimensional updrafts. *Journal of the Atmospheric Sciences*, *73*(11), 4531–4551.

Peters, J. M., Chavas, D. R., Su, C.-Y., Morrison, H., & Coffer, B. E. (2023). An analytic formula for entraining cape in mid-latitude storm environments. *Journal of the Atmospheric Sciences*, *80*(9), 2165–2186.

Peters, J. M., Hannah, W., & Morrison, H. (2019). The influence of vertical wind shear on moist thermals. *Journal of the Atmospheric Sciences*, *76*(6), 1645–1659.

Peters, J. M., Morrison, H., Varble, A. C., Hannah, W. M., & Giangrande, S. E. (2020). Thermal chains and entrainment in cumulus updrafts. Part II: Analysis of idealized simulations. *Journal of the Atmospheric Sciences*, *77*(11), 3661–3681.

Powell, S. W. (2024). Updraft width implications for cumulonimbus growth in a moist marine environment. *Journal of the Atmospheric Sciences*, *81*(3), 629–648.

Prein, A., Gobiet, A., Suklitsch, M., Truhetz, H., Awan, N., Keuler, K., & Georgievski, G. (2013). Added value of convection permitting seasonal simulations. *Climate Dynamics*, *41*, 2655–2677.

Prein, A., Gobiet, A., Truhetz, H., Keuler, K., Goergen, K., Teichmann, C., ... others (2016). Precipitation in the EURO-CORDEX 0.11° and 0. 44° simulations: high resolution, high benefits? *Climate dynamics*, *46*, 383–412.

Randall, D., Khairoutdinov, M., Arakawa, A., & Grabowski, W. (2003). Breaking the cloud parameterization deadlock. *Bulletin of the American Meteorological Society*, *84*(11), 1547 - 1564.

Rio, C., Del Genio, A. D., & Hourdin, F. (2019). Ongoing breakthroughs in convective parameterization. *Current Climate Change Reports*, *5*(2), 95–111.

Satoh, M., Tomita, H., Yashiro, H., Miura, H., Kodama, C., Seiki, T., ... others (2014). The non-hydrostatic icosahedral atmospheric model: Description and development. *Progress in Earth and Planetary Science*, *1*, 1–32.

Savazzi, A. C., Jakob, C., & Siebesma, A. P. (2021). Convective mass-flux from long term radar reflectivities over Darwin, Australia. *Journal of Geophysical Research: Atmospheres*, e2021JD034910.

Schiro, K. A., Ahmed, F., Giangrande, S. E., & Neelin, J. D. (2018). GoAmazon2014/5 campaign points to deep-inflow approach to deep convection across scales. *Proceedings of the National Academy of Sciences*, *115*(18), 4577–4582.

Schneider, T., Leung, L. R., & Wills, R. C. J. (2024). Opinion: Optimizing climate models with process knowledge, resolution, and artificial intelligence. *Atmospheric Chemistry and Physics*, *24*(12), 7041–7062.

Shchepetkin, A. F., & McWilliams, J. C. (1998). Quasi-monotone advection schemes based on explicit locally adaptive dissipation. *Monthly weather review*, *126*(6), 1541–1580.

Shutts, G. J., & Gray, M. E. B. (1994). A numerical modelling study of the geostrophic adjustment process following deep convection. *Quarterly Journal of the Royal Meteorological Society*, *120*(519), 1145–1178.

Siebesma, A. P., Soares, P. M. M., & Teixeira, J. (2007). A combined eddy-diffusivity mass-flux approach for the convective boundary layer. *Journal of the Atmospheric Sciences*, *64*(4), 1230–1248.

Sinha, P., Tiwari, P. R., Kar, S., Mohanty, U., Raju, P., Dey, S., & Shekhar, M. (2015). Sensitivity studies of convective schemes and model resolutions in simulations of wintertime circulation and precipitation over the western himalayas. *Pure and Applied Geophysics*, *172*, 503–530.

Squires, P. (1958). Penetrative downdraughts in cumuli. *Tellus*, *10*(3), 381–389.

Stevens, B., Adami, S., Ali, T., Anzt, H., Aslan, Z., Attinger, S., … Ziemen, F. (2024). Earth Virtualization Engines (EVE). *Earth System Science Data*, *16*(4), 2113–2122.

Stevens, B., Satoh, M., Auger, L., Biercamp, J., Bretherton, C. S., Chen, X., … others (2019). DYAMOND: the DYnamics of the Atmospheric general circulation Modeled On Non-hydrostatic Domains. *Progress in Earth and Planetary Science*, *6*(1), 1–17.

Tarshish, N., Jeevanjee, N., & Lecoanet, D. (2018). Buoyant motion of a turbulent thermal. *Journal of the Atmospheric Sciences*, *75*(9), 3233–3244.

Tomita, H., & Satoh, M. (2004). A new dynamical framework of nonhydrostatic global model using the icosahedral grid. *Fluid Dynamics Research*, *34*(6), 357.

Varble, A., Zipser, E. J., Fridlind, A. M., Zhu, P., Ackerman, A. S., Chaboureau, J.-P., … Shipway, B. (2014). Evaluation of cloud-resolving and limited area model intercomparison simulations using TWP-ICE observations: 1. Deep convective updraft properties. *Journal of Geophysical Research: Atmospheres*, *119*(24), 13–891.

Weisman, M. L., Manning, K. W., Sobash, R. A., & Schwartz, C. S. (2023). Simulations of severe convective systems using 1-versus 3-km grid spacing. *Weather and Forecasting*, *38*(3), 401–423.

Weisman, M. L., Skamarock, W. C., & Klemp, J. B. (1997). The resolution dependence of explicitly modeled convective systems. *Monthly Weather Review*, *125*(4), 527–548.

Wing, A. A., Stauffer, C. L., Becker, T., Reed, K. A., Ahn, M.-S., Arnold, N. P., … others (2020). Clouds and convective self-aggregation in a multimodel ensemble of radiative-convective equilibrium simulations. *Journal of Advances in Modeling Earth Systems*, *12*(9), e2020MS002138.

Wu, C.-M., Lin, H.-C., Cheng, F.-Y., & Chien, M.-H. (2019). Implementation of the land surface processes into a vector vorticity equation model (VVM) to study its impact on afternoon thunderstorms over complex topography in Taiwan. *Asia-Pacific Journal of Atmospheric Sciences*, *55*, 701–717.

Xu, K.-M., Cederwall, R. T., Donner, L. J., Grabowski, W. W., Guichard, F., Johnson, D. E., … Zhang, M.-H. (2002). An intercomparison of cloud-resolving models with the atmospheric radiation measurement summer 1997 intensive observation period data. *Quarterly Journal of the Royal Meteorological Society*, *128*(580), 593-624.

Yanai, M., Esbensen, S., & Chu, J.-H. (1973). Determination of bulk properties of tropical cloud clusters from large-scale heat and moisture budgets. *Journal of Atmospheric Sciences*, *30*(4), 611–627.

Yang, D. (2018). Boundary layer diabatic processes, the virtual effect, and convective self-aggregation. *Journal of Advances in Modeling Earth Systems*, *10*(9), 2163–2176.

Yashiro, H., Kajikawa, Y., Miyamoto, Y., Yamaura, T., Yoshida, R., & Tomita, H. (2016). Resolution dependence of the diurnal cycle of precipitation simulated by a global cloud-system resolving model. *SOLA*, *12*, 272–276.

Zhang, G. J., & McFarlane, N. A. (1995). Sensitivity of climate simulations to the parameterization of cumulus convection in the Canadian Climate Centre general circulation model. *Atmosphere-ocean*, *33*(3), 407–446.

Zhang, Y., & Boos, W. R. (2023). An upper bound for extreme temperatures over midlatitude land. *Proceedings of the National Academy of Sciences*, *120*(12), e2215278120.

Zhou, B., Sun, S., Yao, K., & Zhu, K. (2018). Reexamining the gradient and countergradient representation of the local and nonlocal heat fluxes in the convective boundary layer. *Journal of the Atmospheric Sciences*, *75*(7), 2317–2336.

Diagnosing nonlocal effects and coherent structure scales in moist convection using a large-eddy simulation

Fu-Sheng Kao[1], Yi-Hung Kuo[2*], and Chien-Ming Wu[1]

[1]Department of Atmospheric Sciences, National Taiwan University, Taipei City, Taiwan
[2]Cooperative Institute for Modeling the Earth System, Princeton University, Princeton, NJ, USA

Key Points:

- The anelastic dynamics suggests that the flow acceleration is insensitive to the small-scale variation due to the nonlocal pressure effects
- This is verified by a large-eddy simulation in which the acceleration is robust to the coherent turbulent structures embedded in the flow
- This holds for both the buoyancy and dynamic contributions to the acceleration, and for convective elements including a wide range of scales

*Now at Department of Atmospheric and Oceanic Sciences, University of California, Los Angeles, Los Angeles, CA, USA

Corresponding author: Chien-Ming Wu, mog@as.ntu.edu.tw

Abstract

The anelastic theory of effective buoyancy has been generalized to include the effects of momentum flux convergence. Mediated by the nonlocal perturbation pressure, the dynamics tends to average over details of the forcing, yielding acceleration robust to small-scale variations of the flow. Here we demonstrate in a large-eddy simulation (LES) with a 100-m horizontal grid spacing that including the anelastic nonlocal dynamics can help capture the mean evolution of convection without fully resolving the fine-scale coherent turbulent structures embedded in the flow. Instances of convection in the LES are identified. For these, the buoyancy and dynamic contributions to the vertical momentum tendency are separately diagnosed. The diagnoses show that buoyancy is the leading effect in the vertical acceleration while strongly interacting with the vertical momentum flux convergence. In comparison, the influence of the horizontal momentum flux convergence on the vertical motion are substantially weaker. The sensitivity resulting from averaging over fine-scale features are quantified. For deep-convective cases, these contributions at the cloud scale ($\sim$ 8 km) exhibit a robustness—as measured in a root-mean-square sense—to horizontally smoothing out turbulent features of scales $\lesssim$ 3 km. As expected, such scales depend on the size of the convective element of interest, while dynamic contributions tend to be more susceptible to horizontal smoothing than does the buoyancy contribution. By verifying a key attribute of the pressure-mediated dynamics in an LES, results here lend support to simplifying the representation of moist convection under the anelastic nonlocal framework for global climate models and storm-resolving simulations.

Plain Language Summary

Moist convection is a leading effect in climate dynamics and gives rise to extreme weather events under global warming. Climate adaption and mitigation rely on accurately simulating convection which remains challenging even for state-of-the-art climate models. Recent advances in computing power have permitted high-resolution global models that can partially resolve convective storms. But empirical evidence based on exploratory numerical experiments suggests that the resolution needed for practical climate applications will not become available soon. Latest theoretical studies, on the other hand, point to a possibility that, by properly including the effect of pressure in models, the evolution of convective flows can be reasonably captured without fully resolving the small-scale turbulence. In this work, the theoretically motivated assertion is put to the test against and is substantiated by a realistic simulation of convection. This implies potential for improving the model representation of convection with more feasible resolution options for climate applications.

1 Introduction

Moist convection is essential for the redistribution of heat, moisture, momentum (Houze, 2018), and can greatly impact human society through producing extreme precipitation or inducing heatwaves (Neelin et al., 2022; Y. Zhang & Boos, 2023). The representation of moist convection in global climate models (GCMs) is key to accurately capturing the diurnal variability of precipitation (Covey et al., 2016; Rio et al., 2019; Christopoulos & Schneider, 2021), the onset of convection (Xu et al., 2002; Petch, 2004; Y.-H. Kuo et al., 2020), and mesoscale convective system (MCS) precipitation patterns (Dong et al., 2023). Representing convection in GCMs, however, remains challenging due to insufficient model grid spacings to resolve convective processes (Arakawa, 2004), resulting in biases in simulations and casting uncertainty in climate projections (Randall et al., 2003; Flato et al., 2014; Sinha et al., 2015; Leung et al., 2022).

There have been two common approaches devised for the GCM representation of convection. The first approach couples a GCM with a cloud model with which the effects of subgrid-scale convection are parameterized (Arakawa & Schubert, 1974). For conventional parameterizations, variants of steady plumes have been adapted for cloud models (Yanai et al., 1973; G. J. Zhang & McFarlane, 1995; Bretherton et al., 2004; Siebesma et al., 2007). Alternatively, superparameterization embeds a limited-domain cloud-resolving model (CRM) within each GCM grid cell (Grabowski, 2001; Khairoutdinov et al., 2008; K.-T. Kuo et al., 2020) which produces better variability of convective processes such as the Madden-Julian oscillation (MJO; Benedict & Randall, 2009). The second approach simply uses finer grid spacings to resolve convection (Tomita & Satoh, 2004; Stevens et al., 2024). Recent advances in computing power have enabled cloud-permitting resolutions of a few kilometers for global storm-resolving models (GSRMs; Satoh et al., 2014; Stevens et al., 2019; Wing et al., 2020; Hohenegger et al., 2023) in which improvements are noted in, e.g., the spatial-temporal distribution of precipitation (Hohenegger et al., 2008); the occurrence of extreme rainfall (Chan et al., 2013; Prein et al., 2013; Ban et al., 2014); orographic enhancement of convection (Prein et al., 2016); and the simulation of convective storm organization and propagation in a dynamically consistent manner (Marsham et al., 2013; Weisman et al., 2023). Still, these efforts are more of an exploratory nature and have not yielded satisfactory outcomes for climate applications (Ma et al., 2022; Miura et al., 2023).

While it is straightforward to try to resolve smaller features of interest by refining grid spacing for CRMs (in superparameterization; Grabowski, 2016) and GSRMs—subject to available computing power—the optimal choices of resolution for aspects of convection are yet to be demonstrated (Hohenegger et al., 2020). Prior studies suggested that a horizontal grid spacing $\Delta_h \approx 4$ km could be sufficient for idealized simulations of squall line systems (Weisman et al., 1997) or bulk convergence behavior (Panosetti et al., 2020); capturing the precipitation diurnal cycle would require $\Delta_h \lesssim 2$ km (Yashiro et al., 2016); and accurately reproducing the structural evolution and precipitation of convective storms may need 1-km or sub-kilometers (Miyamoto et al., 2013; Ito et al., 2021). Empirically, the evidence points to even finer grid spacings in both vertical and horizontal that will not soon become feasible for practical climate applications (Jeevanjee & Zhou, 2022; Jenney et al., 2023). As such, traditional parameterizations—preferably with a novel treatment of moist convection—are very much relevant in the foreseeable future for climate projections as well as for a process-level understanding of convection (Schneider et al., 2024).

This raises the question of whether it is possible to capture important aspects of convection without fully resolving the small-scale turbulent features. And, if so, what would be the minimal resolution required for, e.g., simulating deep-convective entities? This manuscript aims to address these questions via a theoretical approach. In doing so, we are motivated by recent studies of effective buoyancy (Tarshish et al., 2018; Y.-H. Kuo & Neelin, 2022; Davies-Jones, 2022) that sought representations of nonhydrostatic pressure effects in convective flows, while leveraging solutions developed in Y.-H. Kuo and Neelin (2024a) and a coordinated large-eddy simulation (LES). Specifically, the analytic expression derived under the anelastic framework indicate that the nonlocal pressure response driven by the buoyancy and momentum flux convergence tends to average over details of the forcing, thus yielding acceleration robust to fine-scale variations of the flow [see Figure 5 in Tarshish et al. (2018), Figure 4 in Y.-H. Kuo and Neelin (2022), and the text therein]. Given the importance of convection as a leading effect in climate change, this theoretical assertion warrants further elaboration aided by realistic simulations of convection, particularly since the robustness of the flow tendency suggests potential for simplifying the representation of the dynamics especially at scales relevant for both large cumulonimbus and MCSs.

Following the groundwork laid in Y.-H. Kuo and Neelin (2024a), here, we diagnose the vertical acceleration within convective regions in an LES and examine the sensitivity of the acceleration to small-scale turbulent features of the flow. As prelude, Section 2 recaps the anelastic nonlocal dynamics, focusing on diagnosing the buoyancy and dynamic contributions to the vertical acceleration. We then briefly overview in Section 3 the setup of the LES experiment in which the acceleration contributions are diagnosed. Section 4 presents the diagnosed vertical mass flux tendency contributions for a selected deep-convective case. The robustness of these contributions to horizontal smoothing for convective features of different sizes are examined in Section 5. Finally, we summarize in Section 6 and discuss potential implications.

2 Anelastic Nonlocal Dynamics: An Overview

To prepare for the analyses presented in subsequent sections, here we follow Y.-H. Kuo and Neelin (2022, 2024a) to recap the diagnostic equation for the nonlocal vertical acceleration. For orientation, note that no approximations are made beyond the anelastic framework in this manuscript.

Assuming the anelastic continuity equation $\nabla\cdot(\rho_0\mathbf{u}) = 0$, where $\rho_0(z)$ is the reference atmospheric density, and $\mathbf{u} \equiv (u, v, w)$ the 3-D velocity field. One can start with the Navier-Stokes equations for $\mathbf{u}$, e.g., Equations 2-4 of Jung and Arakawa (2008)—omitting the eddy ($''$) terms for simplicity—and apply $\nabla\times$ twice to the system; after rearrangement and simplification, the z-component yields

$$\mathcal{L}(a) = \nabla_h^2\left[B - \frac{1}{\rho_0}\nabla\cdot(\rho_0\mathbf{u}w)\right] + D_H, \tag{1}$$

where $a \equiv \partial_t w$ is the Eulerian vertical acceleration, B the buoyancy,

$$\mathcal{L}(a) \equiv \nabla_h^2 a + \frac{\partial}{\partial z}\left[\frac{1}{\rho_0}\frac{\partial}{\partial z}(\rho_0 a)\right], \tag{2}$$

and the higher derivatives of the divergence of horizontal momentum fluxes

$$D_H \equiv \frac{\partial}{\partial z}\left\{\frac{1}{\rho_0}\left[\partial_x\nabla\cdot(\rho_0\mathbf{u}u) + \partial_y\nabla\cdot(\rho_0\mathbf{u}v)\right]\right\}. \tag{3}$$

The buoyancy and dynamic contributions to vertical acceleration can then be diagnosed via Equation 1 as

$$\frac{\partial w}{\partial t} = \underbrace{\mathcal{L}^{-1}\nabla_h^2\left[B \overbrace{- \frac{1}{\rho_0}\nabla\cdot(\rho_0\mathbf{u}w)}^{D_V}\right]}_{a(B)+a(D_V)} \underbrace{+\mathcal{L}^{-1}D_H}_{a(D_H)}, \tag{4}$$

in which $\mathcal{L}^{-1}$ denotes solving Equation 1 with boundary conditions imposed on $\partial_t w$. For simplicity, we use $a(B)$, $a(D_V)$, and $a(D_H)$ to refer to the respective contributions to vertical acceleration by B, D_V, and D_H in subsequent discussion; since ρ_0 is time-independent, we also call $\rho_0 a \equiv \partial_t(\rho_0 w)$ the acceleration and D_V the convergence of vertical momentum, where the meanings are clear from the context.

By comparing Equation 4 here with, e.g., Equation 4 of Jung and Arakawa (2008)—where pressure is expressed in terms of the virtual potential temperature θ_v and *Exner function* π—rearranged as (with c_p the specific heat for air at constant pressure; subscript 0 for a reference state; and prime the respective perturbation)

$$\frac{\partial w}{\partial t} = \underbrace{B - \frac{1}{\rho_0}\nabla\cdot(\rho_0\mathbf{u}w)}_{\textit{Local non-PGF acceleration}} \underbrace{-\frac{\partial}{\partial z}(c_p\theta_{v0}\pi')}_{\textit{PGF}}, \tag{5}$$

we note the following. The elliptic operator $\mathcal{L}(\cdot)$ defined by Equation 2 arises from solving the nonhydrostatic perturbation pressure, and its solution tends to have a vertically and horizontally *nonlocal* influence even if the forcing is localized. This behavior is similar to that seen in, e.g., electrostatics where a point charge can establish an electric field in the surroundings (see also Tarshish et al., 2018). The usage of the term "nonlocal" here, therefore, is different from that in the parameterized up-gradient transport literature (Deardorff, 1966; Holtslag & Moeng, 1991; Siebesma et al., 2007; Zhou et al., 2018; Chor et al., 2021).

On the right-hand side of Equation 4, the first term consists of contributions $a(B)$ and $a(D_V)$ by the buoyancy B and convergence of vertical momentum flux D_V—both of which appear in Equation 5 as the local non-pressure-gradient-force (*non-PGF*) acceleration—that are mediated by the nonlocal perturbation pressure; the second term $a(D_H)$ likewise represents the pressure-driven acceleration resulting from the effect of divergence of horizontal momentum fluxes D_H (recall Equation 3). Thus while Equation 4 appears to be an equation for vertical velocity, it includes the horizontal velocity and continuity equations, and nonlocal effects beyond those represented in *effective buoyancy* [i.e., $a(B)$; see Davies-Jones, 2003; Jeevanjee & Romps, 2016; Peters, 2016].

A key attribute of the nonlocal dynamics is its dependence on dimensions of the convective element (Y.-H. Kuo & Neelin, 2022; Davies-Jones, 2022). Consequently, the solution tends to average over details of the flow, and thus yielding acceleration robust to fine-scale forcing variations. This suggests potential for capturing the evolution of convection without fully resolving the coherent turbulent structures embedded in the flow—the underlying assumption for the simplified representation of the dynamics in the Y.-H. Kuo and Neelin (2024a, 2024b) anelastic convective entity (ACE) model that is yet to be verified quantitatively. To complement and support the theoretical work, this manuscript aims to address the gap by testing the hypothesis using an LES. Specifically, we will examine in the LES the buoyancy and dynamic contributions to vertical acceleration, and quantify their robustness to horizontally smoothing out fine-scale features of the flow.

While it is not possible to cover full treatment here and some aspects of the dynamics must be left for future work, we underlie the following features before turning to the LES setup in the next section. In deriving Equation 4, the eddy terms are omitted for simplicity. Including these would add eddy momentum flux contributions to the dynamic terms D_V, D_H with their impact on the flow exerted through the same mediating pressure effect. In addition, the nonlocal dynamics applies to both the vertical and horizontal acceleration. Recall that Equation 4 (or equivalently, Equation 1) is derived by applying $\nabla\times$ twice to the Navier-Stokes velocity equation and identifying the z-component; the corresponding horizontal component yields an equation akin to Equation 4 from which the horizontal flow tendency can be diagnosed in the same manner.

3 The LES Setup

To diagnose the contributions to vertical acceleration, we use the Vector Vorticity equation cloud-resolving Model or VVM (Jung & Arakawa, 2008; Wu et al., 2019) to produce an LES run. The VVM is a 3-D anelastic model in which the horizontal vorticity is prognostic from which other dynamic variables are inferred; the vertical velocity—being the exception—is directly diagnosed via an elliptic equation with the same operator $\mathcal{L}$ in Equation 2, thus yielding solutions consistent with the diagnostic Equation 4. Such formulation directly couples the flow with buoyancy through vorticity tendency, making the solution responsive to horizontal buoyancy variations for the simulation of convection (see, e.g., K.-T. Kuo & Wu, 2019; Y.-T. Chen & Wu, 2019). In the current implementation, the VVM dynamical core is coupled with additional components including the RRTMG (for radiative transfer; Iacono et al., 2008); the Noah land surface model (F. Chen & Dudhia, 2001); the Shutts and Gray (1994) 1st-order turbulence closure; and the P3 microphysics (Morrison & Milbrandt, 2015; Huang & Wu, 2020). For prior VVM applications, see also Chien and Wu (2016) Hsieh et al. (2022), and Chang et al. (2023).

For the present application, the LES run is performed in a doubly-periodic domain of 102.4 km × 102.4 km in the horizontal with a flat surface ($z = 0$) and a model top at 19.8 km. The grid spacing is $\Delta x = \Delta y = 100$ m in the horizontal, and Δz increases from 75 m at the surface to 150 m near the model top in the vertical. The simulation is initialized using a tropical oceanic sounding adapted from the DYNAMO campaign observations (Gottschalck et al., 2013). A prescribed large-scale subsidence and a weak background southwesterly of 3 m s^{-1} are imposed (without a meaningful vertical wind shear) so that the solution can capture a variety of convective behaviors including both shallow and deep convection. The imposed southwesterly also results in all convective features propagating northeastward. The simulation period covers 9 days with instantaneous fields output every 10 min—including the buoyancy and dynamic forcings B, D_V, D_H and the respective contributions to vertical acceleration $a(B)$, $a(D_V)$, and $a(D_H)$ diagnosed via Equation 4 during the runtime.

In VVM, the total condensate mixing ratio $q_c \equiv q_\ell + q_i + q_r$ (respectively the mixing ratios of cloud liquid water, ice, and rain) and the buoyancy is evaluated including the virtual effects following

$$B \equiv g \left(\frac{\theta - \theta_0}{\theta_0} + 0.608 q_v - q_c \right), \tag{6}$$

where $g = 9.81$ m s^{-2}; θ is the potential temperature; subscript 0 here for the domain-mean profile; and q_v the water vapor mixing ratio.

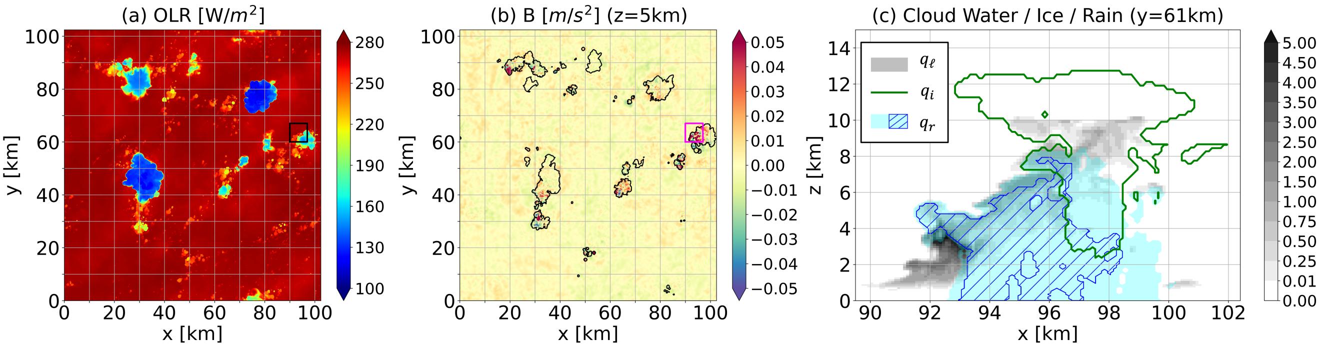

Figure 1. Snapshots at $t = 66$ h 40 m into the VVM simulation for (a) OLR and (b) buoyancy at $z = 5$ km. A developing deep-convective cloud occurs at the boxed location in (a-b) for which the mixing ratios of condensate species at $y = 61$ km are shown in (c), including the cloud liquid water q_ℓ (gray shading in g kg^{-1}), ice q_i (green contours for $q_i = 0.1$ g kg^{-1}), and rain drops q_r (light blue and hatching for q_r exceeding 0.1 and 1 g kg^{-1}, respectively); the total condensate mixing ratio $q_c \equiv q_\ell + q_i + q_r$. Note that a weak background southwesterly is imposed on the solution, resulting in all convective features moving northeastward. The cloud instance in (c) is examined in subsequent figures. The black/magenta square in (a-b) marks a region of 7 km × 7 km in the horizontal, comparable to the current global storm-resolving resolution, and is used to define the mean tendency $\overline{(\cdot)}$.

To give a sense of the VVM simulation, Figure 1 illustrates snapshots at $t = 66$ h 40 m. The outgoing long-wave radiation (OLR) in Figure 1a shows a number of convective clouds at this time, two of which are mature and exhibit extensive high anvils. A few developing instances can be noted in Figure 1b as indicated by the strong buoyancy anomalies at $z = 5$ km. Among these, one is centered near $x = 93$ km and $y = 63$ km for which Figure 1c shows the cross section of condensate mixing ratios q_ℓ (gray shading in g kg^{-1}), q_i (green contour for 0.1 g kg^{-1}), and q_r (light blue and hatching for values exceeding 0.1 and 1 g kg^{-1}, respectively).

The developing instance illustrated in Figure 1c is selected for a case study with additional diagnoses presented through subsequent Figures 2-6. For another case study sampled at a later time $t = 76$ h 40 m yielding consistent results, see Supporting Information. In these two LES timeslices, we also identify all cloud objects of different sizes (see Appendix C for the identifying criteria). These objects are then used to compile the statistics in Figure 7 for demonstrating the dependence on convective feature size.

We are now ready for diagnosing the contributions to vertical acceleration in the LES.

4 Buoyancy and Dynamic Contributions to Vertical Acceleration

For the selected case highlighted in Figure 1, the buoyancy and dynamic forcings B, D_V, D_H and their respective contributions to vertical mass flux tendency $\rho_0 a(B)$, $\rho_0 a(D_V)$, $\rho_0 a(D_H)$ are shown in Figure 2 (as a visual reference, the liquid and ice cloud boundaries are marked by the black and green contours). While the details included in Figure 2 are informative, the mean tendency over the convective region is also of interest given its implications for, e.g., representations of moist convection in GCMs as well as understanding convective processes in GSRMs. In particular, the mean mass flux profile through continuity determines the far-field inflow towards the convective region (Schiro et al., 2018; Savazzi et al., 2021) and the saturated outflow for stratiform cloud formation (Y.-H. Kuo & Neelin, 2024b). As such, we illustrate in Figure 3 the mean tendency contributions—denoted by $\rho_0 \overline{a(\cdot)}$—over a region of 7 km × 7 km in the horizontal (marked by a square in Figure 1a,b) comparable to a current GSRM grid cell.

In Figure 2a, the cross section shows the primary positive buoyancy feature emerging between $x = 90$ and 97 km in the liquid-cloud region, exhibiting a chain of rising thermals (Varble et al., 2014; Morrison et al., 2020; Peters et al., 2020). Near the surface, a cold pool yields negative values of buoyancy. The convective cold-top negative buoyancy can also be seen near the top of the (ice) cloud (Holloway & Neelin, 2007; Li et al., 2022), likely due to the combined effect of the mixing-driven evaporative cooling (Squires, 1958; Paluch, 1979; Blyth, 1993) and the vertically nonlocal upward acceleration causing adiabatic cooling (Y.-H. Kuo & Neelin, 2022, 2024a). Figure 2d shows the buoyancy-driven vertical mass flux tendency $\rho_0 a(B) \equiv \rho_0 \mathcal{L}^{-1}\nabla_h^2 B$—recall Equation 4—including both the Archimedean buoyancy and its associated perturbation pressure effect. Overall, the sign of the tendency matches that of the buoyancy. But because of the nonlocal dynamics interacting with the surface boundary condition $\partial_t w = 0$, the near-surface tendency tends to have small values despite the cold-pool negative buoyancy. In addition, if one were to overlay Figure 2a,d, the mass flux tendency would appear to be smoother than the buoyancy (see also Figures 4d and 5d).

Figure 2b shows $D_V \equiv -\rho_0^{-1}\nabla \cdot (\rho_0 \mathbf{u} w)$ with the corresponding mass flux tendency $\rho_0 a(D_V) \equiv \mathcal{L}^{-1}\nabla_h^2 D_V$ in Figure 2e. Compared with the buoyancy, both D_V and $\rho_0 a(D_V)$ exhibit smaller-scale features due to sign reversal in velocity in coherent turbulent structures embedded in the flow, e.g., vortex rings associated with rising thermals. Larger values also tend to be confined within the cloud. While the magnitude in Figure 2b,e appears to be stronger than that of the buoyancy, substantial cancellation can occur when the forcing/tendency is averaged over the cloud region.

Finally, Figure 2c,f illustrates the cross sections of D_H and $\rho_0 a(D_H) \equiv \mathcal{L}^{-1} D_H$. Recall Equation 3 that D_H includes higher derivatives of the divergence of horizontal momentum fluxes, hence has units different from those of B and D_V. This also results in D_H exhibiting even finer-scale features than D_V in Figure 2b. The corresponding $\rho_0 a(D_H)$ in Figure 2f seems less noisy than D_H due to the nonlocal effect.

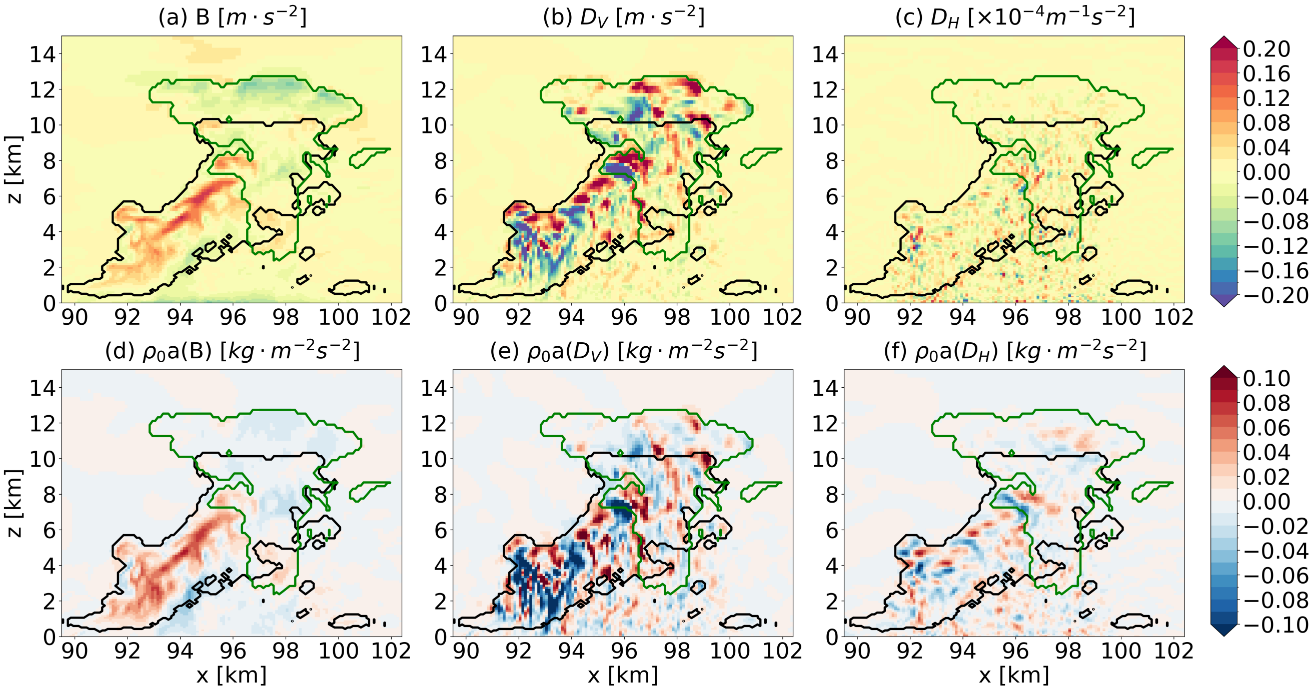

Figure 2. The buoyancy and dynamic forcings that yield the nonlocal vertical acceleration, including contributions by (a) the buoyancy (B), (b) the vertical (D_V) and (c) horizontal momentum flux divergence (D_H); the respective vertical mass flux tendencies $\rho_0 a(B)$, $\rho_0 a(D_V)$, and $\rho_0 a(D_H)$ are in (d-f). Note that the units of D_H in (c) are different from those for (a-b). Cross sections here are sampled from $y = 61$ km at $t = 66$ h 40 m into the VVM simulation, with the black/green contours marking the liquid/ice cloud boundaries as shown in Figure 1c.

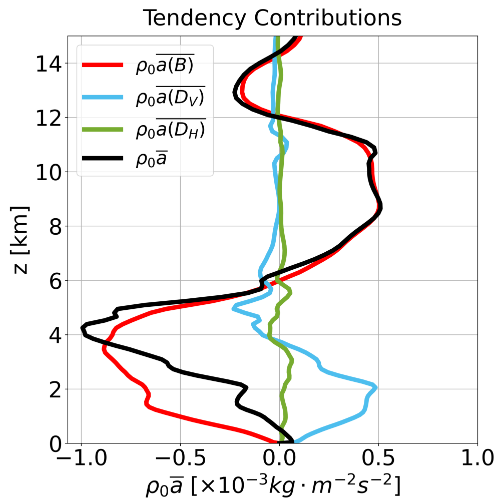

Figure 3. The individual and total contributions to the vertical mass flux tendency horizontally averaged over a 7 km × 7 km region (see the black/magenta square in Figure 1a,b). Solutions here are for the same case illustrated in Figure 2.

The overall magnitude of $\rho_0 a(D_H)$ is notably weaker than $\rho_0 a(B)$, $\rho_0 a(D_V)$ in Figure 2d,e. This is also demonstrated by Figure 3 in which these terms are horizontally averaged over a 7 km × 7 km box enclosing the convective region indicated by strong buoyancy. The total mean tendency (black line) is dominated by the buoyancy contribution (red), exhibiting an upward acceleration between $z = 6$ and 12 km and a downward tendency above and below. That $\partial_t \partial_z(\rho_0 \overline{w}) = \partial_z(\rho_0 \overline{a}) > 0$ for $4 < z < 8$ km implies the far-field inflow towards the convective region is strengthening (or equivalently, the outflow is weakening) in the mid-troposphere. The dynamic contribution has a modest impact on the total tendency—mostly through D_V (blue). In contrast, the effect of D_H (green) appears to be negligible.

For another deep-convective case examined in the same manner, see Supporting Information. While the precise distributions of the forcing and tendency can vary from case to case, the relative importance of B, D_V, and D_H noted here seems to hold in general.

Next, we turn to the robustness of the vertical mass flux tendency to fine-scale features of the flow.

5 Robustness to Coherent Turbulent Structure

This section focuses on the robustness of the nonlocal dynamics. Specifically, we test the assertion that the evolution of convection can be captured without fully resolving the turbulent flow structures. To this end, we apply a horizontal Gaussian filter to the forcing to even out features finer than a prescribed *smoothing scale* s, and then examine the sensitivity of the nonlocal acceleration to the smoothing. For more details on Gaussian smoothing, see Appendix B.

5.1 Dependence on horizontal smoothing scale

Figure 4 shows the cross sections of B, D_V, D_H and their filtered counterparts denoted by $\widetilde{(\cdot)}$. The column on the left repeats Figure 2a-c and the middle two columns illustrate results filtered with $s = 0.9$ and 2.4 km. The rightmost column includes the mean forcing profiles averaged over the 7 km × 7 km region—the same used for Figure 3—for selected values of s (results before smoothing are included and labeled as 100m). The corresponding contributions to vertical mass flux tendency are shown in Figure 5.

As noted earlier, the buoyancy includes scales comparable to the size of the cloud in which the coherent structures are embedded (Figure 4a), thus exhibiting a robustness to smoothing (Figure 4b-c). Even with $s = 2.4$ km, the filtered buoyancy $\widetilde{B}$ shows a pattern resembling the original snapshot before filtering. When these are horizontally averaged over the 7 km × 7 km region, the resulting profiles in Figure 4d are virtually indistinguishable from the original until s well exceeds 3 km. These findings hold for the buoyancy-driven tendency in Figure 5a-d as well. In addition, it is worth reiterating that the nonlocal dynamics applies not only horizontally but also vertically, as is demonstrated by the profiles in Figure 5d tending to be smoother than those of the buoyancy in Figure 4d.

In comparison with buoyancy, the dynamic contributions in Figure 4e-l and Figure 5e-l include features of smaller scales hence are more susceptible to smoothing. While deviations of the filtered results become substantial for larger values of s ($\gtrsim$ 2.4 km), the mean profiles—especially for the vertical mass flux tendencies in Figure 5h,l—remain robust in both the horizontal and vertical.

The dependence on smoothing of the total and individual contributions to the mass flux tendency is summarized in Figure 6 by showing $\|\rho_0\overline{a(\cdot)} - \rho_0\overline{a(\widetilde{\cdot})}\|_2 / \|\rho_0\overline{a(\cdot)}\|_2$—the normalized root-mean-square (RMS) difference between the mean tendency profiles before and after filtering—as a function of s. Here $\|\cdot\|_2$ denotes the Euclidean norm, and the difference is normalized (using the norm before filtering) so that the value would not

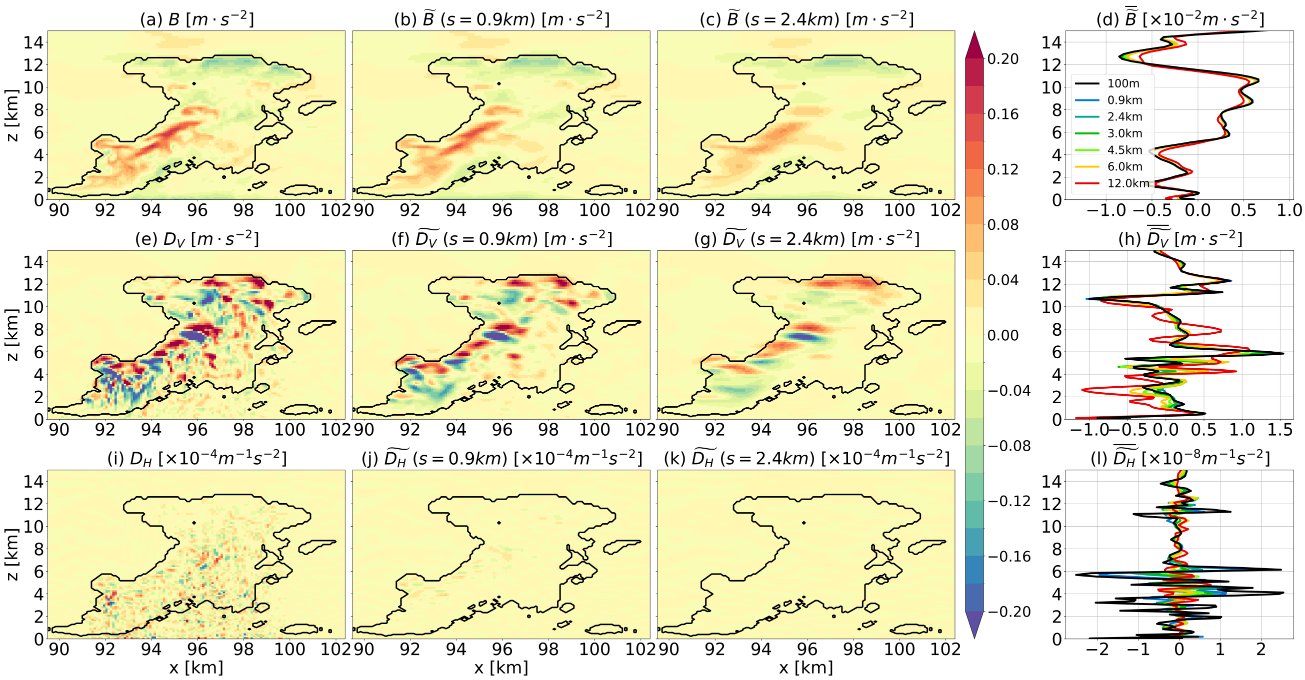

Figure 4. The dependence of the buoyancy and dynamic forcing contributions to horizontal smoothing. (a) The VVM snapshot of buoyancy B as in Figure 2a and (b-c) the horizontally-smoothed buoyancy field $\widetilde{B}$ using a 2-D Gaussian filter with smoothing scales $s = 0.9$ nd 2.4 km to remove the coherent turbulent structure embedded in the flow; the mean profiles of B (black line) and $\widetilde{B}$ (colored lines; for a few values of s in km) horizontally averaged over the 7 km $\times$ 7 km box (see Figure 1a-b) are summarized in (d). (e-h) Same as (a-d) but for the dynamic contribution D_V by the vertical momentum flux convergence; (i-l) Same as (e-h) but for D_H associated with horizontal momentum flux convergence. Note that in (d), (h) and (l) results before smoothing are marked as 100m in the legend.

be impacted by the magnitude of individual contributions. For the selected case, filtering yields solutions with small deviations for the total tendency (black line) and buoyancy contribution (red line) while the dynamic terms (blue and green lines) are less robust with substantially larger deviations. Despite the deviation is most notable for the D_H-induced tendency, the magnitude of the tendency is small and thus tends to have a limited impact on the flow evolution.

5.2 Cloud-size dependence and morphology

Two important aspects have to be considered as we move from the selected example to a variety of instances of convection. First, the robustness of the mean tendency profiles seen in Figure 5d,h,l is not an artifact arising from the interaction between the convolution $\widetilde{(\cdot)}$ and horizontal averaging $\overline{(\cdot)}$. The smoothing scale $s \sim 3$ km at which the deviations of the filtered solutions start to pick up is not sensitive to the size of the domain (e.g., 7 km $\times$ 7 km) over which the horizontal mean is computed (not shown). Instead, this threshold scale varies primarily with the forcing morphology as demonstrated by Figure 6: the threshold tends to be larger for forcing with a simple structure (e.g., B in Figure 4a) while distributions having multiple extrema across a short distance (D_V,

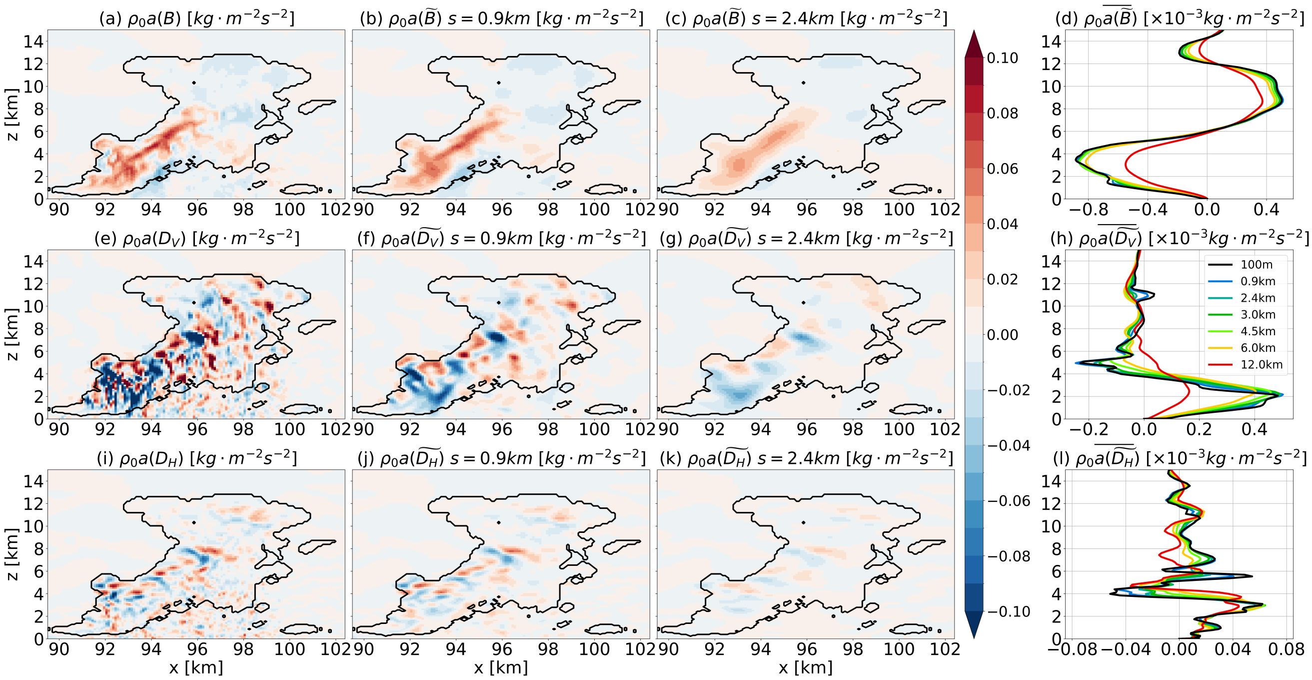

Figure 5. Same as Figure 4 but showing the respective vertical mass flux tendency.

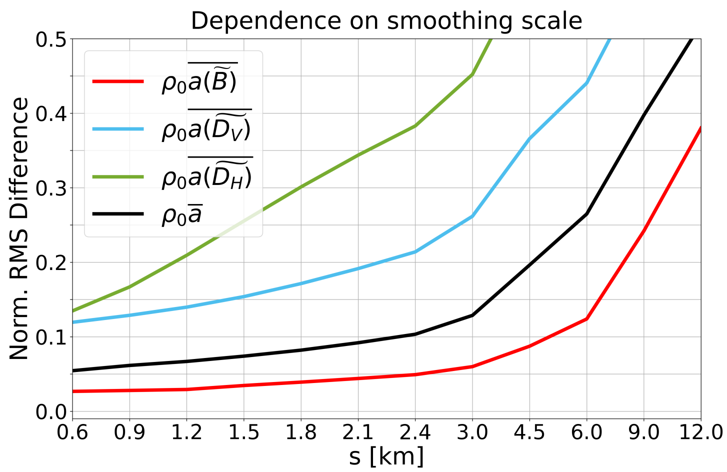

Figure 6. Normalized root-mean-square (RMS) differences between the mean profiles of the VVM vertical mass flux tendency $\rho_0\overline{a(\cdot)}$ and the horizontally-smoothed tendency $\rho_0\overline{a(\widetilde{\cdot})}$, contributed by the individual and total forcings. Here, the differences are normalized by the RMS of the tendency profiles $\rho_0\overline{a(\cdot)}$ before smoothing. Note that the x-axis here showing selected values of s is not on a linear scale.

D_H in Figure 4e,i) tend to yield a smaller threshold. Second, the dependence on cloud size must be assessed.

To address this, Figure 7 repeats the analysis displayed in Figure 6 for a collection of 185 cloud samples of different sizes identified in two LES timeslices that are 10 hours apart at $t = 66$ h 40 m and 76 h 40 m (see Appendix C for the identifying criteria and

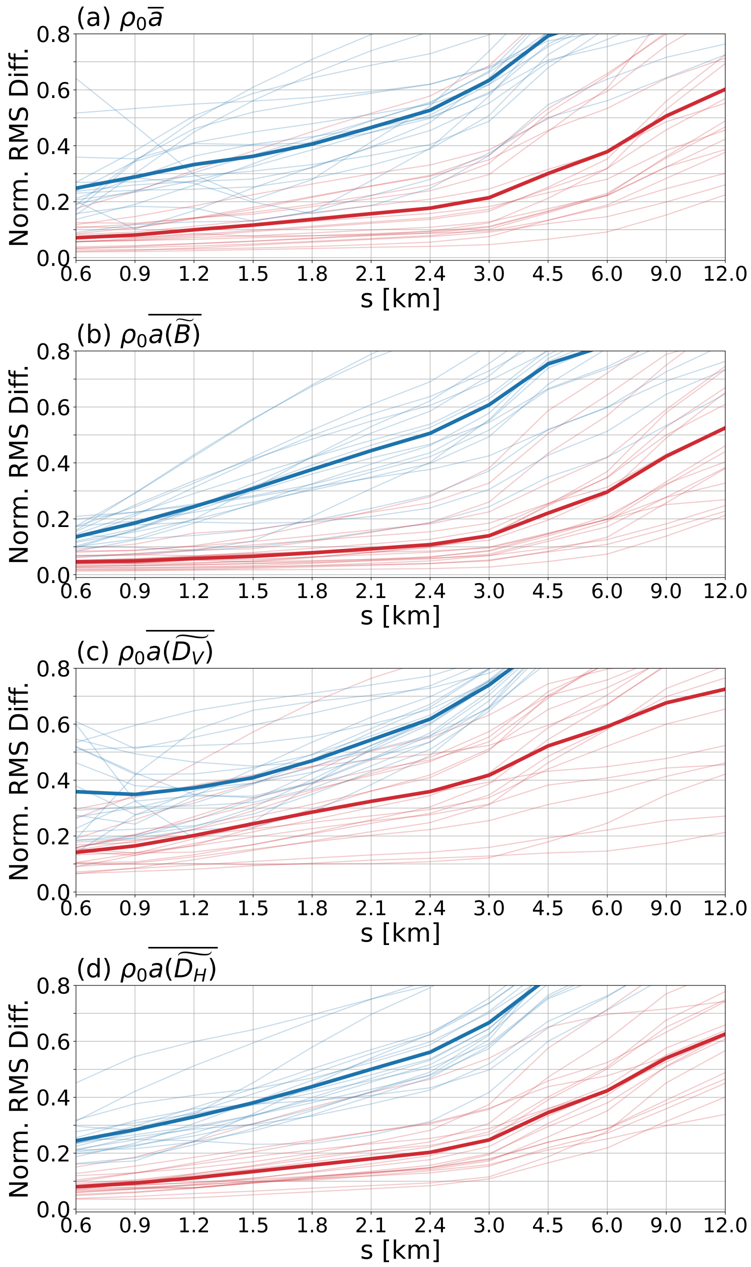

Figure 7. Same as Figure 6, illustrating for an ensemble of clouds of different horizontal sizes (see Appendix C for the measure of size). The light red lines show the dependence of the normalized RMS difference on the smoothing scale for individual cloud instances whose size is in the top 10% ($\geq$ 7.8 km), while the results for the bottom 10% ($\leq$ 0.8 km) are in light blue. The thick red and blue lines represent the respective means for each category.

the proxy used to measure the cloud size). The normalized RMS differences for the tendency contributions are shown as a function of the smoothing scale for individual clouds in the top (light red lines) and bottom 10% (light blue lines) of the size distribution, together with their respective means for each size group (thick red/blue lines; the 10th- and 90th-percentiles of the cloud size are 0.8 and 7.8 km). The total and buoyancy contributions tend to exhibit smaller differences due to smoothing than do the dynamic contributions; and larger cloud objects systematically yield smaller differences than smaller ones. While fine-scale variations not accounted for by the size proxy can give rise to deviation from the mean, results here are consistent with our intuition built upon earlier illustrations.

6 Summary and Discussion

Under the anelastic framework, this manuscript examines the vertical acceleration field mediated by the nonlocal perturbation pressure. The buoyancy and dynamic contributions to the acceleration are diagnosed in an LES of 100-m horizontal grid spacing that simulates a variety of convective features. For these, the buoyancy contribution $a(B)$—known as the effective buoyancy (Davies-Jones, 2003)—tends to dominate the evolution of the mean flow while interacting with the *effective dynamic acceleration* $a(D_V)$ (Y.-H. Kuo & Neelin, 2024a) of a comparable magnitude driven by the convergence of vertical momentum flux. The contribution $a(D_H)$ associated with divergence of horizontal momentum fluxes, in contrast, is at least an order smaller in magnitude thus only has a limited impact on the mean flow.

Results compiled with cloud objects sampled from the LES indicate that the diagnosed contributions to the vertical acceleration tend to be robust to horizontally filtering out fine-scale variations embedded in the flow. Because larger convective entities include coherent structures of larger scales than do smaller clouds, the nonlocal acceleration resulting from larger entities is less susceptible to the smoothing. This is demonstrated by the mean acceleration profiles for selected deep-convective cases exhibiting little variation, measured in root-mean-square differences, before and after the horizontal filtering until the smoothing scale exceeds a threshold of ~ 3 km. As expected, the threshold is systematically smaller for convective features of smaller sizes though deviations from the mean may be seen among individual instances. Also, dynamic contributions exhibit more sensitivity to smoothing than the buoyancy contribution. Although we have focused on the mean tendencies over convective regions, the effect of smaller-scale eddies on tracer transport cannot be overlooked (Jeevanjee & Zhou, 2022; Jenney et al., 2023); the scales associated with coherent flows noted here could facilitate a more consistent treatment for partitioning the mean-flow and eddy contributions.

While the analysis framework in this manuscript is purely diagnostic, it could aid in understanding convective processes for simplified representations in GCMs and GSRMs. Y.-H. Kuo and Neelin (2024b) have illustrated that the approximation $\partial_t w \approx a(B) + a(D_V)$ [i.e., omitting $a(D_H)$] in time-varying solutions for convective updraft tends to spawn off a chain of rising thermals especially in the upper part of the updraft—results here support the use of such approximation. It follows as a corollary that steady plumes are unlikely to be an effective description for convective drafts. Apart from contributing to the overall mixing, the spontaneously-generated thermals can also act as a source of gravity waves in a manner that differs from a steady-updraft solution for parameterized processes such as gravity wave drag (Kim et al., 2003; Beres et al., 2004; Alexander et al., 2021). More generally, the representations of moist/shallow convection in a GCM or GSRM should begin to move away from typical steady-state assumption, or to at least consider these time-dependent aspects.

In addition, horizontal size has recently been recognized as a key factor distinguishing small cloud embryos that grow into deep convection from those do not (Powell, 2024). A greater embryo size favors convective growth by simultaneously reducing entrainment mixing and enhancing the nonlocal effects (Y.-H. Kuo & Neelin, 2024a); solutions here can help discern the relative importance of these two pathways. Including a background wind shear or vorticity can substantially alter the flow evolution (Peters et al., 2019; LeBel & Markowski, 2023; Peters et al., 2023) but its interaction with the nonlocal dynamics will be an endeavor for future work. The onset of convective aggregation is another subject of interest for which the up-gradient transport of boundary layer moist static energy (MSE) due to virtual temperature effect is a leading contribution (Yang, 2018; Huang & Wu, 2022); diagnoses presented here might provide useful ways to quantify the transfers of MSE helping clarify the mechanism.

In light of the results, the point here is not so much about a particular threshold scale, but that aspects of the evolution of convection can be represented without fully resolving the turbulent flow. This inherent feature of the anelastic nonlocal dynamics previously noted in theoretical studies such as Tarshish et al. (2018), Y.-H. Kuo and Neelin (2022), and Davies-Jones (2022) now has an LES underpinning supporting process-level modeling of convection for GCMs and GSRMs.

Appendix A An alternative diagnostic equation for (p, T)-system

This work relies on the VVM LES in which (π, θ) is used in lieu of pressure p and temperature T (Jung & Arakawa, 2008), and thus our presentation of the nonlocal diagnostic equation follows the same approach. The corresponding equation for the alternative (p, T) anelastic system has been covered in Y.-H. Kuo and Neelin (2024a) which is included for completeness:

$$\partial_t(\rho_0 w) = \nabla^{-2}\nabla_h^2\big[\rho_0 B - \nabla\cdot(\rho_0 \mathbf{u} w)\big] + \nabla^{-2}D'_H, \tag{A1}$$

where

$$D'_H \equiv \partial_z\big[\partial_x \nabla\cdot(\rho_0\mathbf{u}u) + \partial_y\nabla\cdot(\rho_0\mathbf{u}v)\big]. \tag{A2}$$

The operator $\mathcal{L}$ defined via Equation 2 is replaced by a 3-D Laplacian ∇^2 here with ∇^{-2} denoting solving the Poisson equation. While the change of variables yields simpler expressions, it does not inherently alter the nonlocal dynamics.

Appendix B Gaussian smoothing

To test the robustness of the nonlocal acceleration, in Section 5 we apply a horizontal convolution to filter out fine-scale features of the flow (similar to the smoothing procedure in Shchepetkin & McWilliams, 1998). Specifically, for a variable $f(x, y, z)$ of interest, the filtered field is given by

$$\widetilde{f}(x,y,z) \equiv \iint G(x',y')f(x-x', y-y', z)dx'dy', \tag{B1}$$

where

$$G(x,y) \equiv \frac{1}{2\pi\sigma^2}e^{-(x^2+y^2)/2\sigma^2} \tag{B2}$$

is the 2-D Gaussian kernel. For a given $\sigma > 0$, $G(x, y)$ drops to $\sim 1\%$ of its peak value for $r \equiv \sqrt{x^2+y^2} \approx 3\sigma$. Hence features smaller than the *smoothing scale* $s \equiv 6\sigma$ tend to be filtered out by the convolution—s is used as a measure for the horizontal smoothing for results included in Section 5.

Note that convolution is a linear operation, thus preserves the relation between the forcing and acceleration contributions, i.e., $a(\widetilde{\cdot}) = \widetilde{a(\cdot)}$. For instance, applying a Gaussian filter with $s = 0.9$ km to the $\rho_0 a(B)$ illustrated in Figure 5a would yield a smoothed solution $\rho_0\widetilde{a(B)}$ that is identical to the $\rho_0 a(\widetilde{B})$ in Figure 5b; the identity holds for the D_V and D_H contributions as well. In principle, this property holds for other linear filters among which the *boxcar* filter corresponding to coarse-graining may be of interest. Nonetheless, we note that (1) the Gaussian smoothing and coarse-graining *should* yield similar results; and (2) the spectral property of the boxcar function *could* produce spurious computational artifacts when the filtering is followed by solving an elliptic equation. As such, the Gaussian smoothing is used for simplicity.

In Figures 4-7, the filtered results are computed by first evaluating B, D_V, D_H via Equations 3-4 and 6 using the LES output, and then applying the Gaussian smoothing. An alternative procedure—as is commonly applicable to considerations of subgrid-scale representations (Leonard, 1975; Moeng, 1984)—applies the Gaussian smoothing to the LES output before computing the forcings. This yields

$$\begin{aligned}\widetilde{D_V}' &\equiv -\frac{1}{\rho_0}\nabla\cdot(\rho_0\widetilde{\mathbf{u}}\widetilde{w}),\\ \widetilde{D_H}' &\equiv \frac{\partial}{\partial z}\left\{\frac{1}{\rho_0}\left[\partial_x\nabla\cdot(\rho_0\widetilde{\mathbf{u}}\widetilde{u})+\partial_y\nabla\cdot(\rho_0\widetilde{\mathbf{u}}\widetilde{v})\right]\right\},\end{aligned} \tag{B3}$$

which can subsequently be substituted into Equation 4 in lieu of D_V, D_H to solve for the acceleration contributions (for completeness, buoyancy is omitted from Equation B3 since its expression does not include nonlinear terms, hence filtering first does not alter the outcome). It is worth noting that the two filtering procedures yield reasonably consistent outcomes, as demonstrated in Figure B1 which compares the two procedures by showing results for the primary contribution $B + D_V$.

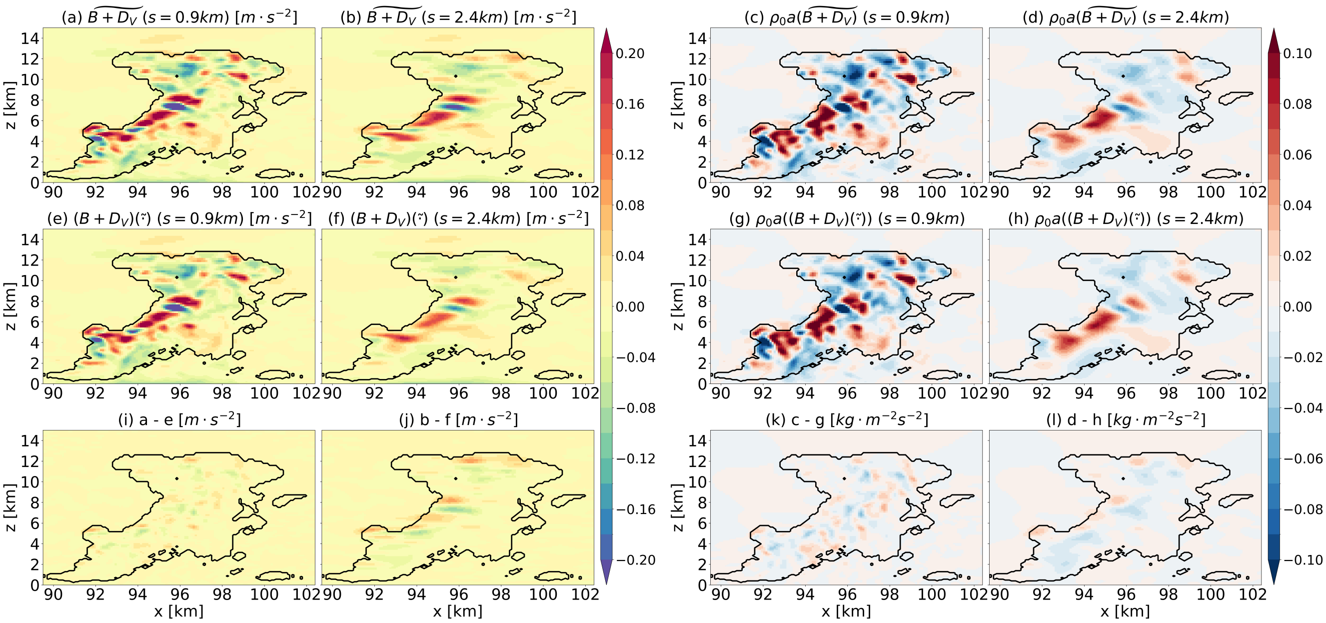

Figure B1. Differences in the smoothed forcing and vertical mass flux tendency due to the filtering procedures. (a-d) Smoothed variables by applying the filter after evaluating $B + D_V$ from the raw LES output. (e-h) The corresponding results computed by applying the filter first using Equation B3. (i-l) Respective differences between (a-d) and (e-h).

In Figure B1, the first row includes the smoothed forcing and vertical mass flux tendency computed by applying the filter after evaluation (i.e., the same procedure for Figures 4-5) while the second row exhibits results for applying the filter first (that is, Equation B3); their differences are illustrated in the bottom row (e.g., Figure B1i shows the difference between panels a and e). In short, while the deviation tends to increase with the smoothing scale, the outcome demonstrates only a modest sensitivity to the filtering procedures.

Appendix C Identifying cloud objects

To infer the relationship between feature size and the robustness of the nonlocal dynamics to smoothing, we identify cloud objects from the LES timeslices and diagnose for each cloud object the buoyancy and dynamic contributions to vertical flow acceleration. The identifying criteria are as follows.

Recall in, e.g., Figure 1a,b that mature clouds with extensive anvils are not necessarily associated with a strong buoyancy or flow velocity. Hence to focus on cases presenting strong forcings, we define a (liquid) cloud object as a connected component of $q_\ell > 0$ in which $w > 5$ m s^{-1} for at least one LES grid point. Each object identified this way is then enclosed by a rectangular column; denoting by A the minimal horizontal area of such columns with which $\sqrt{A}$ is used as a proxy for the object size. This proxy is used to compile the cloud size distribution for the statistics shown in Figure 7 for which the mean mass flux tendencies $\rho_0\overline{a(\cdot)}$ are averaged over the minimal horizontal area A.

Acknowledgments

This work was supported by the Princeton AOS Postdoctoral Research Scientists Program under award NA18OAR4320123 from the National Oceanic and Atmospheric Administration, U.S. Department of Commerce (YHK), and by the National Science and Technology Council of Taiwan through Grants 113-2111-M-002-001- to National Taiwan University (FSK and CMW). We are grateful for comments from Drs. Wei-Ting Chen, Leo J. Donner, James C. McWilliams, and J. David Neelin that helped improve this work.

Data Availability Statement

The VVM source code is publicly available at https://github.com/chienmingwu/VVM, and the LES output can be accessed via https://doi.org/10.5281/zenodo.13317028 together with the analysis and plotting scripts for this manuscript.

References

Alexander, M. J., Liu, C. C., Bacmeister, J., Bramberger, M., Hertzog, A., & Richter, J. H. (2021). Observational validation of parameterized gravity waves from tropical convection in the Whole Atmosphere Community Climate Model. *Journal of Geophysical Research: Atmospheres*, *126*(7), e2020JD033954.

Arakawa, A. (2004). The cumulus parameterization problem: Past, present, and future. *Journal of Climate*, *17*(13), 2493 - 2525.

Arakawa, A., & Schubert, W. H. (1974). Interaction of a cumulus cloud ensemble with the large-scale environment, Part I. *Journal of Atmospheric Sciences*, *31*(3), 674–701.

Ban, N., Schmidli, J., & Schär, C. (2014). Evaluation of the convection-resolving regional climate modeling approach in decade-long simulations. *Journal of Geophysical Research: Atmospheres*, *119*(13), 7889–7907.

Benedict, J. J., & Randall, D. A. (2009). Structure of the madden–julian oscillation in the superparameterized cam. *Journal of the Atmospheric Sciences*, *66*(11), 3277–3296.

Beres, J. H., Alexander, M. J., & Holton, J. R. (2004). A method of specifying the gravity wave spectrum above convection based on latent heating properties and background wind. *Journal of the atmospheric sciences*, *61*(3), 324–337.

Blyth, A. M. (1993). Entrainment in cumulus clouds. *Journal of Applied Meteorology and Climatology*, *32*(4), 626–641.

Bretherton, C. S., McCaa, J. R., & Grenier, H. (2004). A new parameterization for shallow cumulus convection and its application to marine subtropical cloud-topped boundary layers. Part I: Description and 1D results. *Monthly Weather Review*, *132*(4), 864–882.

Chan, S. C., Kendon, E. J., Fowler, H. J., Blenkinsop, S., Ferro, C. A., & Stephenson, D. B. (2013). Does increasing the spatial resolution of a regional climate model improve the simulated daily precipitation? *Climate dynamics*, *41*, 1475–1495.

Chang, Y.-H., Chen, W.-T., Wu, C.-M., Kuo, Y.-H., & Neelin, J. D. (2023). Identifying the deep-inflow mixing features in orographically-locked diurnal convection. *Geophysical Research Letters*, *50*(10), e2023GL103107.

Chen, F., & Dudhia, J. (2001). Coupling an advanced land surface–hydrology model with the Penn State–NCAR MM5 modeling system. Part I: Model implementation and sensitivity. *Monthly weather review*, *129*(4), 569–585.

Chen, Y.-T., & Wu, C.-M. (2019). The role of interactive SST in the cloud-resolving simulations of aggregated convection. *Journal of Advances in Modeling Earth Systems*, *11*(10), 3321–3340.

Chien, M.-H., & Wu, C.-M. (2016). Representation of topography by partial steps using the immersed boundary method in a vector vorticity equation model (VVM). *Journal of Advances in Modeling Earth Systems*, *8*(1), 212-223.

Chor, T., McWilliams, J. C., & Chamecki, M. (2021). Modifications to the K-profile parameterization with nondiffusive fluxes for Langmuir turbulence. *Journal of Physical Oceanography*, *51*(5), 1503–1521.

Christopoulos, C., & Schneider, T. (2021). Assessing biases and climate implications of the diurnal precipitation cycle in climate models. *Geophysical Research Letters*, *48*(13), e2021GL093017.

Covey, C., Gleckler, P. J., Doutriaux, C., Williams, D. N., Dai, A., Fasullo, J., ... Berg, A. (2016). Metrics for the diurnal cycle of precipitation: Toward routine benchmarks for climate models. *Journal of Climate*, *29*(12), 4461–4471.

Davies-Jones, R. (2003). An expression for effective buoyancy in surroundings with horizontal density gradients. *Journal of the Atmospheric Sciences*, *60*(23), 2922–2925.

Davies-Jones, R. (2022). An analytical solution of the effective-buoyancy equation. *Journal of the Atmospheric Sciences*, *79*(12), 3135–3144.

Deardorff, J. W. (1966). The counter-gradient heat flux in the lower atmosphere and in the laboratory. *Journal of the Atmospheric Sciences*, *23*(5), 503–506.

Dong, W., Zhao, M., Ming, Y., Krasting, J. P., & Ramaswamy, V. (2023). Simulation of united states mesoscale convective systems using gfdl's new high-resolution general circulation model. *Journal of Climate*, *36*(19), 6967 - 6990.

Flato, G., Marotzke, J., Abiodun, B., Braconnot, P., Chou, S. C., Collins, W., ... others (2014). Evaluation of climate models. In *Climate change 2013: the physical science basis. Contribution of Working Group I to the Fifth Assessment Report of the Intergovernmental Panel on Climate Change* (pp. 741–866). Cambridge University Press.

Gottschalck, J., Roundy, P. E., Schreck III, C. J., Vintzileos, A., & Zhang, C. (2013). Large-scale atmospheric and oceanic conditions during the 2011–12 DYNAMO field campaign. *Monthly Weather Review*, *141*(12), 4173–4196.

Grabowski, W. W. (2001). Coupling cloud processes with the large-scale dynamics using the cloud-resolving convection parameterization (CRCP). *Journal of the Atmospheric Sciences*, *58*(9), 978–997.

Grabowski, W. W. (2016). Towards global large eddy simulation: Super-parameterization revisited. *Journal of the Meteorological Society of Japan. Ser. II*, *94*(4), 327–344.

Hohenegger, C., Brockhaus, P., & Schar, C. (2008). Towards climate simulations at cloud-resolving scales. *Meteorologische Zeitschrift*, *17*(4), 383–394.

Hohenegger, C., Korn, P., Linardakis, L., Redler, R., Schnur, R., Adamidis, P., ... Stevens, B. (2023). ICON-Sapphire: simulating the components of the Earth

system and their interactions at kilometer and subkilometer scales. *Geoscientific Model Development*, *16*(2), 779–811.
Hohenegger, C., Kornblueh, L., Klocke, D., Becker, T., Cioni, G., Engels, J. F., ... Stevens, B. (2020). Climate statistics in global simulations of the atmosphere, from 80 to 2.5 km grid spacing. *Journal of the Meteorological Society of Japan. Ser. II*, *98*(1), 73–91.
Holloway, C. E., & Neelin, J. D. (2007). The convective cold top and quasi equilibrium. *Journal of the Atmospheric Sciences*, *64*(5), 1467–1487.
Holtslag, A. A. M., & Moeng, C.-H. (1991). Eddy diffusivity and countergradient transport in the convective atmospheric boundary layer. *Journal of the Atmospheric Sciences*, *48*(14), 1690–1698.
Houze, R. A. (2018). 100 years of research on mesoscale convective systems. *Meteorological Monographs*, *59*, 17–1.
Hsieh, M.-K., Chen, Y.-W., Chen, Y.-C., & Wu, C.-M. (2022). The roles of local circulation and boundary layer development in tracer transport over complex topography in central Taiwan. *Journal of the Meteorological Society of Japan. Ser. II*, *100*(3), 555–573.
Huang, J.-D., & Wu, C.-M. (2020). Effects of microphysical processes on the precipitation spectrum in a strongly forced environment. *Earth and Space Science*, *7*(6), e2020EA001190.
Huang, J.-D., & Wu, C.-M. (2022). A framework to evaluate convective aggregation: Examples with different microphysics schemes. *Journal of Geophysical Research: Atmospheres*, *127*(5), e2021JD035886.
Iacono, M. J., Delamere, J. S., Mlawer, E. J., Shephard, M. W., Clough, S. A., & Collins, W. D. (2008). Radiative forcing by long-lived greenhouse gases: Calculations with the AER radiative transfer models. *Journal of Geophysical Research: Atmospheres*, *113*(D13).
Ito, J., Tsuguchi, H., Hayashi, S., & Niino, H. (2021). Idealized high-resolution simulations of a back-building convective system that causes torrential rain. *Journal of the Atmospheric Sciences*, *78*(1), 117–132.
Jeevanjee, N., & Romps, D. M. (2016). Effective buoyancy at the surface and aloft. *Quarterly Journal of the Royal Meteorological Society*, *142*(695), 811–820.
Jeevanjee, N., & Zhou, L. (2022). On the resolution-dependence of anvil cloud fraction and precipitation efficiency in radiative-convective equilibrium. *Journal of Advances in Modeling Earth Systems*, *14*(3), e2021MS002759.
Jenney, A. M., Ferretti, S. L., & Pritchard, M. S. (2023). Vertical resolution impacts explicit simulation of deep convection. *Journal of Advances in Modeling Earth Systems*, *15*(10), e2022MS003444.
Jung, J.-H., & Arakawa, A. (2008). A three-dimensional anelastic model based on the vorticity equation. *Monthly Weather Review*, *136*(1), 276–294.
Khairoutdinov, M., DeMott, C., & Randall, D. (2008). Evaluation of the simulated interannual and subseasonal variability in an AMIP-style simulation using the CSU multiscale modeling framework. *Journal of Climate*, *21*(3), 413–431.
Kim, Y.-J., Eckermann, S. D., & Chun, H.-Y. (2003). An overview of the past, present and future of gravity-wave drag parametrization for numerical climate and weather prediction models. *Atmosphere-Ocean*, *41*(1), 65–98.
Kuo, K.-T., Wei-Ting, C., & Chien-Ming, W. (2020). Effects of convection-SST interactions on the South China Sea summer monsoon onset in a multiscale modeling framework model. *TAO: Terrestrial, Atmospheric and Oceanic Sciences*, *31*(2), 2.
Kuo, K.-T., & Wu, C.-M. (2019). The precipitation hotspots of afternoon thunderstorms over the Taipei Basin: Idealized numerical simulations. *Journal of the Meteorological Society of Japan. Ser. II*, *97*(2), 501–517.
Kuo, Y.-H., & Neelin, J. D. (2022). Conditions for convective deep inflow. *Geophysical Research Letters*, *49*, e2022GL100552.

Kuo, Y.-H., & Neelin, J. D. (2024a). Anelastic Convective Entities. Part 1: Formulation and implication for nighttime convection. *Authorea Preprints*.

Kuo, Y.-H., & Neelin, J. D. (2024b). Anelastic Convective Entities. Part 2: Adjustment processes and convective cold top. *Authorea Preprints*.

Kuo, Y.-H., Neelin, J. D., Booth, J. F., Chen, C.-C., Chen, W.-T., Gettelman, A., … Zhao, M. (2020). Convective transition statistics over tropical oceans for climate model diagnostics: GCM evaluation. *Journal of Atmospheric Sciences*, *77*, 379-403.

LeBel, L. J., & Markowski, P. M. (2023). An analysis of the impact of vertical wind shear on convection initiation using large-eddy simulations: Importance of wake entrainment. *Monthly Weather Review*, *151*(7), 1667–1688.

Leonard, A. (1975). Energy cascade in large-eddy simulations of turbulent fluid flows. In *Advances in Geophysics* (Vol. 18, pp. 237–248). Elsevier.

Leung, L. R., Boos, W. R., Catto, J. L., A. DeMott, C., Martin, G. M., Neelin, J. D., … others (2022). Exploratory precipitation metrics: Spatiotemporal characteristics, process-oriented, and phenomena-based. *Journal of Climate*, *35*(12), 3659–3686.

Li, Y.-X., Neelin, J. D., Kuo, Y.-H., Hsu, H.-H., & Yu, J.-Y. (2022). How close are leading tropical tropospheric temperature perturbations to those under convective quasi equilibrium? *Journal of the Atmospheric Sciences*, *79*(9), 2307–2321.

Ma, H.-Y., Klein, S. A., Lee, J., Ahn, M.-S., Tao, C., & Gleckler, P. J. (2022). Superior daily and sub-daily precipitation statistics for intense and long-lived storms in global storm-resolving models. *Geophysical Research Letters*, *49*(8), e2021GL096759.

Marsham, J. H., Dixon, N. S., Garcia-Carreras, L., Lister, G. M. S., Parker, D. J., Knippertz, P., & Birch, C. E. (2013). The role of moist convection in the West African monsoon system: Insights from continental-scale convection-permitting simulations. *Geophysical Research Letters*, *40*(9), 1843–1849.

Miura, H., Suematsu, T., Kawai, Y., Yamagami, Y., Takasuka, D., Takano, Y., … Masumoto, Y. (2023). Asymptotic matching between weather and climate models. *Bulletin of the American Meteorological Society*, *104*(12), E2308 - E2315.

Miyamoto, Y., Kajikawa, Y., Yoshida, R., Yamaura, T., Yashiro, H., & Tomita, H. (2013). Deep moist atmospheric convection in a subkilometer global simulation. *Geophysical Research Letters*, *40*(18), 4922-4926.

Moeng, C.-H. (1984). A large-eddy-simulation model for the study of planetary boundary-layer turbulence. *Journal of the Atmospheric Sciences*, *41*(13), 2052–2062.

Morrison, H., & Milbrandt, J. A. (2015). Parameterization of cloud microphysics based on the prediction of bulk ice particle properties. Part I: Scheme description and idealized tests. *Journal of the Atmospheric Sciences*, *72*(1), 287–311.

Morrison, H., Peters, J. M., Varble, A. C., Hannah, W. M., & Giangrande, S. E. (2020). Thermal chains and entrainment in cumulus updrafts. Part I: Theoretical description. *Journal of the Atmospheric Sciences*, *77*(11), 3637–3660.

Neelin, J. D., Martinez-Villalobos, C., Stechmann, S. N., Ahmed, F., Chen, G., Norris, J. M., … Lenderink, G. (2022). Precipitation extremes and water vapor: Relationships in current climate and implications for climate change. *Current Climate Change Reports*, *8*(1), 17–33.

Paluch, I. R. (1979). The entrainment mechanism in Colorado cumuli. *Journal of Atmospheric Sciences*, *36*(12), 2467–2478.

Panosetti, D., Schlemmer, L., & Schär, C. (2020). Convergence behavior of idealized convection-resolving simulations of summertime deep moist convection over land. *Climate Dynamics*, *55*(1), 215–234.

Petch, J. C. (2004). The predictability of deep convection in cloud-resolving simulations over land. *Quarterly Journal of the Royal Meteorological Society*, *130*(604), 3173-3187.

Peters, J. M. (2016). The impact of effective buoyancy and dynamic pressure forcing on vertical velocities within two-dimensional updrafts. *Journal of the Atmospheric Sciences*, *73*(11), 4531–4551.

Peters, J. M., Chavas, D. R., Su, C.-Y., Morrison, H., & Coffer, B. E. (2023). An analytic formula for entraining cape in mid-latitude storm environments. *Journal of the Atmospheric Sciences*, *80*(9), 2165–2186.

Peters, J. M., Hannah, W., & Morrison, H. (2019). The influence of vertical wind shear on moist thermals. *Journal of the Atmospheric Sciences*, *76*(6), 1645–1659.

Peters, J. M., Morrison, H., Varble, A. C., Hannah, W. M., & Giangrande, S. E. (2020). Thermal chains and entrainment in cumulus updrafts. Part II: Analysis of idealized simulations. *Journal of the Atmospheric Sciences*, *77*(11), 3661–3681.

Powell, S. W. (2024). Updraft width implications for cumulonimbus growth in a moist marine environment. *Journal of the Atmospheric Sciences*, *81*(3), 629–648.

Prein, A., Gobiet, A., Suklitsch, M., Truhetz, H., Awan, N., Keuler, K., & Georgievski, G. (2013). Added value of convection permitting seasonal simulations. *Climate Dynamics*, *41*, 2655–2677.

Prein, A., Gobiet, A., Truhetz, H., Keuler, K., Goergen, K., Teichmann, C., ... others (2016). Precipitation in the EURO-CORDEX 0.11° and 0. 44° simulations: high resolution, high benefits? *Climate dynamics*, *46*, 383–412.

Randall, D., Khairoutdinov, M., Arakawa, A., & Grabowski, W. (2003). Breaking the cloud parameterization deadlock. *Bulletin of the American Meteorological Society*, *84*(11), 1547 - 1564.

Rio, C., Del Genio, A. D., & Hourdin, F. (2019). Ongoing breakthroughs in convective parameterization. *Current Climate Change Reports*, *5*(2), 95–111.

Satoh, M., Tomita, H., Yashiro, H., Miura, H., Kodama, C., Seiki, T., ... others (2014). The non-hydrostatic icosahedral atmospheric model: Description and development. *Progress in Earth and Planetary Science*, *1*, 1–32.

Savazzi, A. C., Jakob, C., & Siebesma, A. P. (2021). Convective mass-flux from long term radar reflectivities over Darwin, Australia. *Journal of Geophysical Research: Atmospheres*, e2021JD034910.

Schiro, K. A., Ahmed, F., Giangrande, S. E., & Neelin, J. D. (2018). GoAmazon2014/5 campaign points to deep-inflow approach to deep convection across scales. *Proceedings of the National Academy of Sciences*, *115*(18), 4577–4582.

Schneider, T., Leung, L. R., & Wills, R. C. J. (2024). Opinion: Optimizing climate models with process knowledge, resolution, and artificial intelligence. *Atmospheric Chemistry and Physics*, *24*(12), 7041–7062.

Shchepetkin, A. F., & McWilliams, J. C. (1998). Quasi-monotone advection schemes based on explicit locally adaptive dissipation. *Monthly weather review*, *126*(6), 1541–1580.

Shutts, G. J., & Gray, M. E. B. (1994). A numerical modelling study of the geostrophic adjustment process following deep convection. *Quarterly Journal of the Royal Meteorological Society*, *120*(519), 1145–1178.

Siebesma, A. P., Soares, P. M. M., & Teixeira, J. (2007). A combined eddy-diffusivity mass-flux approach for the convective boundary layer. *Journal of the Atmospheric Sciences*, *64*(4), 1230–1248.

Sinha, P., Tiwari, P. R., Kar, S., Mohanty, U., Raju, P., Dey, S., & Shekhar, M. (2015). Sensitivity studies of convective schemes and model resolutions in simulations of wintertime circulation and precipitation over the western himalayas. *Pure and Applied Geophysics*, *172*, 503–530.

Squires, P. (1958). Penetrative downdraughts in cumuli. *Tellus*, *10*(3), 381–389.

Stevens, B., Adami, S., Ali, T., Anzt, H., Aslan, Z., Attinger, S., … Ziemen, F. (2024). Earth Virtualization Engines (EVE). *Earth System Science Data*, *16*(4), 2113–2122.

Stevens, B., Satoh, M., Auger, L., Biercamp, J., Bretherton, C. S., Chen, X., … others (2019). DYAMOND: the DYnamics of the Atmospheric general circulation Modeled On Non-hydrostatic Domains. *Progress in Earth and Planetary Science*, *6*(1), 1–17.

Tarshish, N., Jeevanjee, N., & Lecoanet, D. (2018). Buoyant motion of a turbulent thermal. *Journal of the Atmospheric Sciences*, *75*(9), 3233–3244.

Tomita, H., & Satoh, M. (2004). A new dynamical framework of nonhydrostatic global model using the icosahedral grid. *Fluid Dynamics Research*, *34*(6), 357.

Varble, A., Zipser, E. J., Fridlind, A. M., Zhu, P., Ackerman, A. S., Chaboureau, J.-P., … Shipway, B. (2014). Evaluation of cloud-resolving and limited area model intercomparison simulations using TWP-ICE observations: 1. Deep convective updraft properties. *Journal of Geophysical Research: Atmospheres*, *119*(24), 13–891.

Weisman, M. L., Manning, K. W., Sobash, R. A., & Schwartz, C. S. (2023). Simulations of severe convective systems using 1-versus 3-km grid spacing. *Weather and Forecasting*, *38*(3), 401–423.

Weisman, M. L., Skamarock, W. C., & Klemp, J. B. (1997). The resolution dependence of explicitly modeled convective systems. *Monthly Weather Review*, *125*(4), 527–548.

Wing, A. A., Stauffer, C. L., Becker, T., Reed, K. A., Ahn, M.-S., Arnold, N. P., … others (2020). Clouds and convective self-aggregation in a multimodel ensemble of radiative-convective equilibrium simulations. *Journal of Advances in Modeling Earth Systems*, *12*(9), e2020MS002138.

Wu, C.-M., Lin, H.-C., Cheng, F.-Y., & Chien, M.-H. (2019). Implementation of the land surface processes into a vector vorticity equation model (VVM) to study its impact on afternoon thunderstorms over complex topography in Taiwan. *Asia-Pacific Journal of Atmospheric Sciences*, *55*, 701–717.

Xu, K.-M., Cederwall, R. T., Donner, L. J., Grabowski, W. W., Guichard, F., Johnson, D. E., … Zhang, M.-H. (2002). An intercomparison of cloud-resolving models with the atmospheric radiation measurement summer 1997 intensive observation period data. *Quarterly Journal of the Royal Meteorological Society*, *128*(580), 593-624.

Yanai, M., Esbensen, S., & Chu, J.-H. (1973). Determination of bulk properties of tropical cloud clusters from large-scale heat and moisture budgets. *Journal of Atmospheric Sciences*, *30*(4), 611–627.

Yang, D. (2018). Boundary layer diabatic processes, the virtual effect, and convective self-aggregation. *Journal of Advances in Modeling Earth Systems*, *10*(9), 2163–2176.

Yashiro, H., Kajikawa, Y., Miyamoto, Y., Yamaura, T., Yoshida, R., & Tomita, H. (2016). Resolution dependence of the diurnal cycle of precipitation simulated by a global cloud-system resolving model. *SOLA*, *12*, 272–276.

Zhang, G. J., & McFarlane, N. A. (1995). Sensitivity of climate simulations to the parameterization of cumulus convection in the Canadian Climate Centre general circulation model. *Atmosphere-ocean*, *33*(3), 407–446.

Zhang, Y., & Boos, W. R. (2023). An upper bound for extreme temperatures over midlatitude land. *Proceedings of the National Academy of Sciences*, *120*(12), e2215278120.

Zhou, B., Sun, S., Yao, K., & Zhu, K. (2018). Reexamining the gradient and countergradient representation of the local and nonlocal heat fluxes in the convective boundary layer. *Journal of the Atmospheric Sciences*, *75*(7), 2317–2336.

JAMES

Supporting Information for

Diagnosing nonlocal effects and coherent structure scales in moist convection using a large-eddy simulation

Fu-Sheng Kao,[1] Yi-Hung Kuo,[2]* and Chien-Ming Wu[1]

[1]Department of Atmospheric Sciences, National Taiwan University, Taipei City, Taiwan
[2]Cooperative Institute for Modeling the Earth System, Princeton University, Princeton, NJ, USA

Contents of this file

S1. Diagnosing vertical acceleration for an alternative deep-convective case

In the main text, we have examined in detail the buoyancy and dynamic contributions to the vertical acceleration for a deep-convective case selected from the LES simulation. Here, we provide another deep-convective example and repeat in Figure S1-S3 the analyses shown in Figures 1-3 in the main text. While these two selected instances exhibit quantitative differences, they lead to consistent conclusions.

Specifically, the buoyancy contribution tends to dominate the overall acceleration while strongly interacting with the convergence of vertical momentum flux. In contrast, the contribution associated with divergence of horizontal momentum fluxes only has a limited impact on the acceleration.

*Now at Department of Atmospheric and Oceanic Sciences, University of California, Los Angeles, Los Angeles, CA, USA

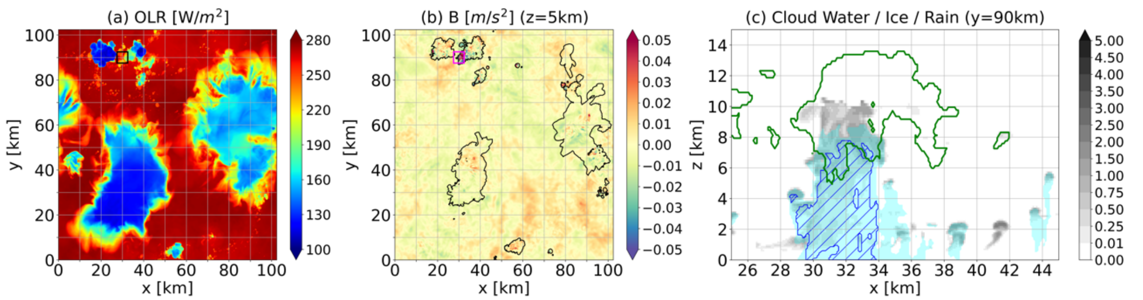

Figure S1. Snapshots similar to Figure 1 in the main text, but for t = 76 h 40 m into the VVM simulation. (a) OLR and (b) buoyancy at z = 5 km. A developing deep-convective cloud occurs at the boxed location in (a-b) for which the mixing ratios of condensate species at y = 90 km are shown in (c), including the cloud liquid water q_ℓ (gray shading in g kg^{-1}), ice q_i (green contours for q_i = 0.1 g kg^{-1}), and rain drops q_r (light blue and hatching for q_r exceeding 0.1 and 1 g kg^{-1}, respectively).The cloud instance in (c) is examined in subsequent Figures S2-S3. The black/magenta square in (a-b) marks a region of 5 km x 5 km in the horizontal and is used to define the mean tendency $\overline{(\cdot)}$ in Figure S3.

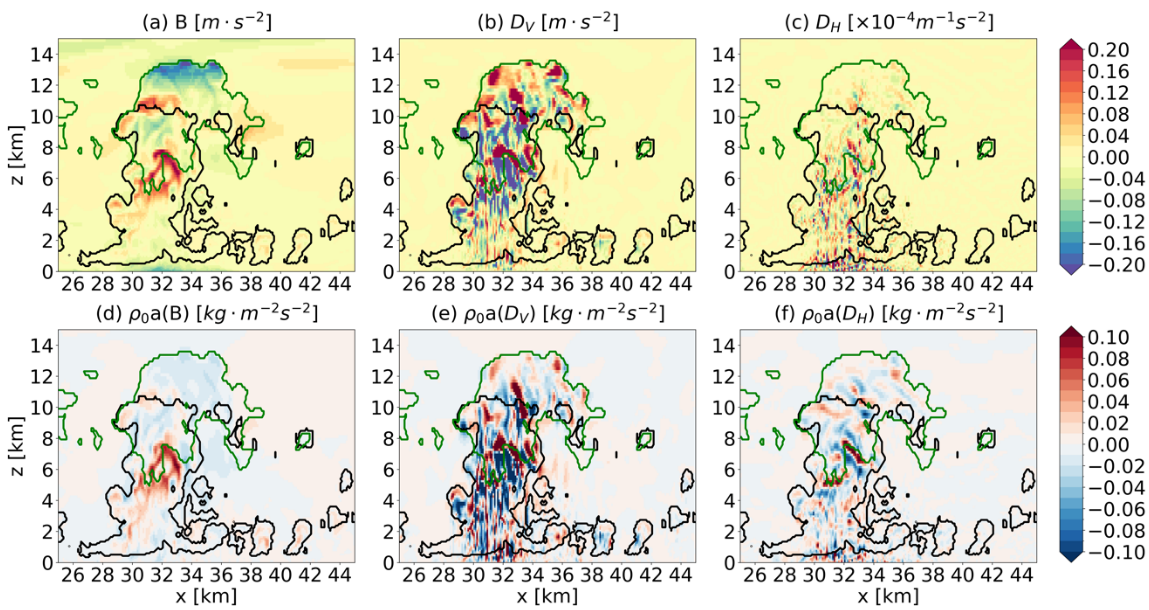

Figure S2. Cross sections similar to Figure 2 in the main text, but for the deep-convective case highlighted in Figure S1c, showing the buoyancy and dynamic forcings that yield the nonlocal vertical acceleration, including contributions by (a) the buoyancy (B), (b) the vertical (D_V) and (c) horizontal momentum flux divergence (D_H); the respective vertical mass flux tendencies $\rho_0 a(B)$, $\rho_0 a(D_V)$, and $\rho_0 a(D_H)$ are in (d-f). Cross sections here are sampled from y = 90 km, with the black/green contours marking the liquid/ice cloud boundaries as shown in Figure S1c.

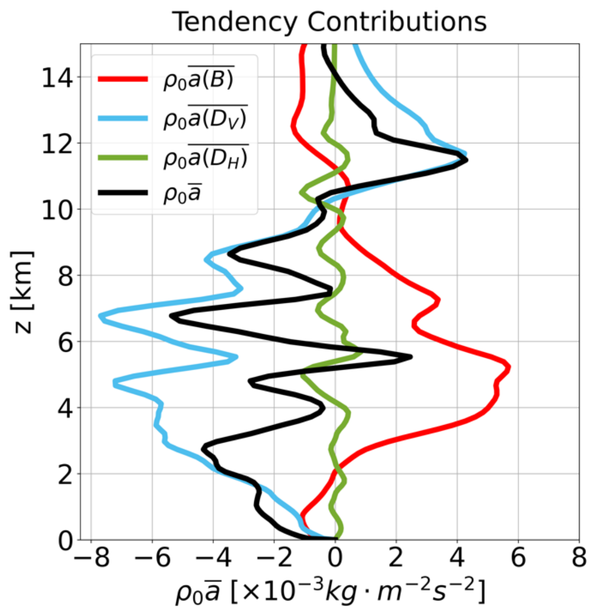

Figure S3. The individual and total contributions to the vertical mass flux tendency horizontally averaged over a 5 km x 5 km region (see the black/magenta square in Figure S1a,b). Solutions here are for the same case illustrated in Figure S2.